Pore Pressure Diffusion and Onset of Induced Seismicity

by

Scott Stokes

B.S., California State University Chico, 2020


A thesis submitted to the

Faculty of the Graduate School of the

University of Colorado in partial fulfillment

of the requirement for the degree of

Master of Science

Department of Geological Sciences

2022


Committee Members:

Dr. Shemin Ge

Dr. Anne Sheehan

Dr. Kristy Tiampo

# Abstract

Stokes, Scott (M.S., Geological Sciences)

Pore Pressure Diffusion and Onset of Induced Seismicity

Thesis directed by Professor Shemin Ge

The Raton Basin of Southern Colorado and Northern New Mexico experienced a significant increase in seismicity over the last several decades, including two M5+ earthquakes. The increase in seismicity started soon after an increase in wastewater injection in the late 1990s. Twenty-nine wastewater injection wells have operated in the Basin, with several high-rate injectors located within a kilometer of the most seismically active regions. We developed a pore pressure model to investigate the relationship between pore pressure diffusion and onset of induced seismicity, with an emphasis on the Trinidad fault zones. Our model indicates that sufficient pore pressure increase had accumulated on the northern extent of the Trinidad fault zone to induce seismicity at the time of early-stage seismic activity. The hydrogeologic architecture of the Basin played a key role in controlling pore pressure perturbation. The basal sedimentary interval with moderately low diffusivity restricted vertical pore pressure diffusion, creating a substantial lag time between wells becoming active and the expression of perturbation in the fault zones. The spatiotemporal relationship between early-stage seismicity and wastewater injection in conjunction with modeled pore pressures suggests that the early-stage seismicity in the Raton Basin was likely triggered by pore pressure diffusion.

# Acknowledgments

Thank you to family, friends, advisors, and fellow graduate students for the support you have provided me throughout graduate school. Thank you to my committee members and counterparts for the time you have dedicated to my graduate research: Shemin Ge, Anne Sheehan, Kristy Tiampo, Megan Brown, Elizabeth Menezes, and Cameron Chambers. I particularly thank you for the effort you all put in to editing my work. A special thank you to Shemin Ge for the copious amounts of time and effort you have dedicated to both my research and development as a hydrogeologist. You have served as a mentor, teaching me technical skills while also serving as an example of how to be a professional, these skills will serve me for the rest of my career. Thank you to my fellow graduate students, particularly Stephen Sheehan, Cameron Chambers and Claudia Corona, for your technical and emotional support throughout my graduate schooling. To my family, thank you for the immeasurable effort you put into raising me and providing me with the platform to succeed, without your efforts I am certain I would not be where I am today.

# Table of Contents

# Tables

# Figures

# 1. Introduction

Deep wastewater injection has been cited as a cause of induced seismicity since the 1960's Rocky Mountain Arsenal earthquakes (Healy et al., 1968) and is recognized as the most likely type of injection to induce seismicity (Weingarten et al., 2015). Several studies have shown that small magnitude stress changes (0.01 – 0.1 MPa) can perturb a critically stressed fault enough to cause failure (Reasenberg and Simpson, 1992; Stein, 1999). Wastewater injection has been shown to produce anthropogenic perturbation that exceeds the stress change needed to reactivate a critically stressed fault (e.g., Brown et al., 2017; Goebel et al., 2017; Hornbach et al., 2015; Keranen et al., 2014; Zhang et al., 2013).

A commonly cited triggering mechanism associated with wastewater injection is pore pressure diffusion. Pore pressure diffusion results in increased pore pressure along a critically stressed fault that reduces effective normal stress, bringing the fault closer to failure (Healy et al., 1968; Hubbert and Rubey, 1959). When critically stressed faults are close to injection wells, and there is a hydraulic connection between the injection interval and seismogenic zone, pore pressure diffusion has been cited as a dominant triggering mechanism (e.g., Chang and Segall, 2016; Goebel et al., 2017). In this study we relate pore pressure diffusion to early-stage seismicity in the Raton Basin where the seismically active regions are near the injectors (Figure 1). Early-stage seismicity is defined as the first M3+ earthquakes to be recorded on previously quiescent faults after injection has started.
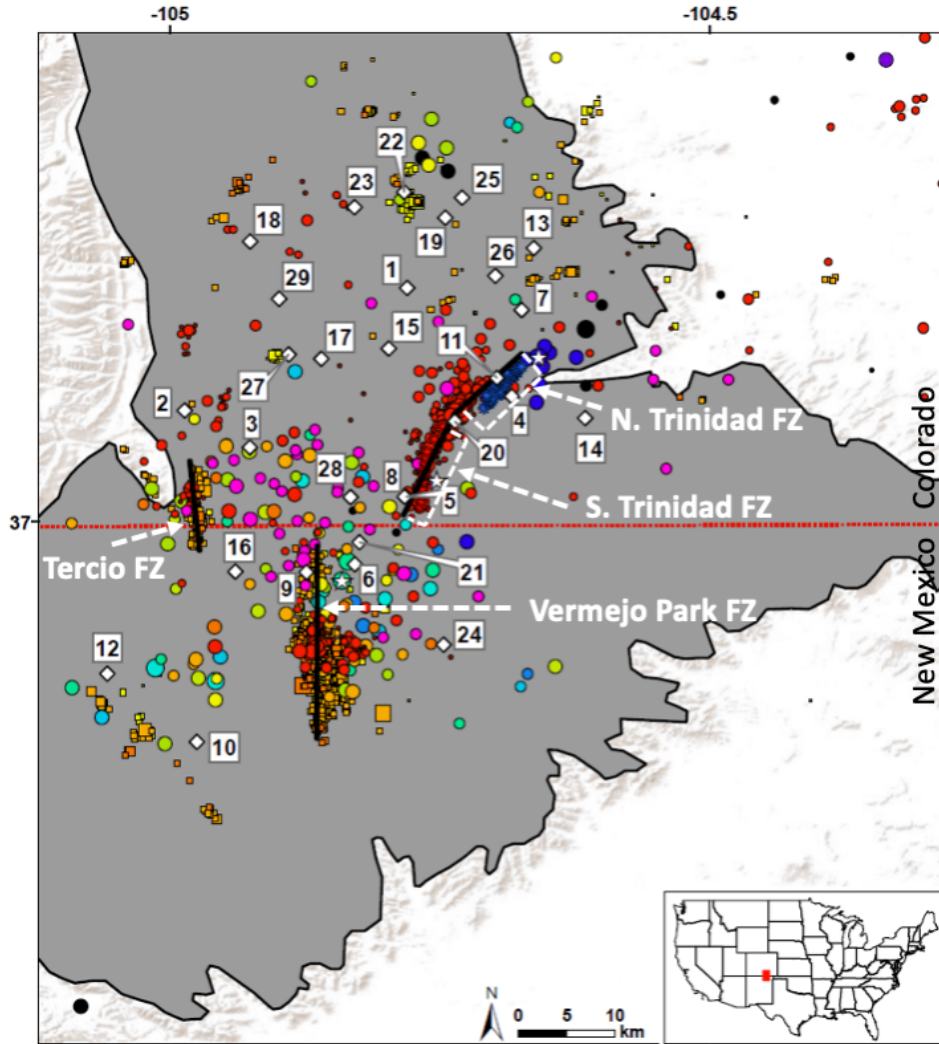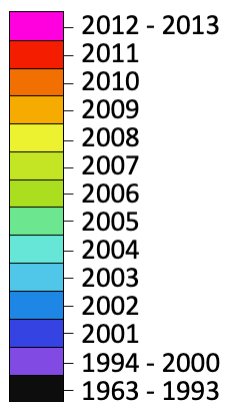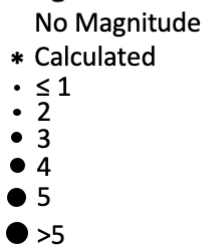
**Figure 1.** Study site location. Grey shaded area denotes Raton Basin. Wastewater disposal wells (white diamonds) labelled by age (1 = oldest well), Rubinstein et al. (2014) catalog of earthquakes from 1963 – 2013 colored by year and sized by earthquake magnitude (circles), Nakai et al. (2017a) catalog of earthquakes from 2008 – 2010 from the EarthScope Transportable array stations colored by year and sized by earthquake magnitude (squares), three studied fault zones (black lines).

The Raton Basin, located on the Colorado-New Mexico border (Figure 1), hosts both coal-bed methane extraction and wastewater injection. Coal-bed methane is exploited from the upper stratigraphy while wastewater injection is conducted over a kilometer deeper (Figure 2; Colorado Oil and Gas Conservation Commission [COGCC], 2020; New Mexico Oil Conservation Division [NMOCD], 2020), separated by the ~ 1 km thick Pierre shale (Baltz, 1965). Wastewater injection started in Colorado in 1994 and New Mexico in 1999; a total of twenty-nine injection wells have operated over the last several decades (COGCC, 2020; NMOCD, 2020). Injection predominantly targets the permeable sedimentary rock of the Dakota formation at ~ 2 km deep (COGCC, 2020; NMOCD, 2020). Below the injection interval lies the Permian-Pennsylvania basal sedimentary units (Figure 2) that separates the injection interval from the Precambrian basement (Robinson et al., 1964). On average, the Precambrian basement is 3 km deep and contains normal faulting (Herrmann, 2020).

Starting in 2001, the Raton Basin experienced a significant increase in seismicity coinciding with an increase in wastewater injection (Figure 3). There was a 40-fold increase in M3.8+ earthquakes when comparing seismicity from 1970 – July 2001 to August 2001 – 2013 (Rubinstein et al., 2014). Since the start of injection, seismicity has predominately been concentrated on three fault zones surrounded by injection wells (Figure 1). Two of the fault zones have recorded significant earthquake sequences. The Trinidad fault zone housed the August-September 2001 sequence and the August-September 2011 sequence (Rubinstein et al., 2014). The Vermejo Park fault zone is suggested to have housed the August-September 2005 sequence (Nakai et al., 2017b). The August-September 2001 sequence marked the start of the Basin's increased

seismicity (Rubinstein et al., 2014). The sequence occurred on the northern extent of the Trinidad fault zone (N. Trinidad fault zone) and was highlighted by a $M_{bLg}$ 4.5 earthquake on 5 September 2001 (Figure 1). The August-September 2005 occurred just south of the Colorado-New Mexico border. The sequence was highlighted by a $M_{wc}$ 5.0 earthquake on 10 August 2005 and is believed to have occurred on the northern extent of the Vermejo Park fault zone (Nakai et al., 2017b). The August-September 2011 sequence occurred on the southern extent of the Trinidad fault zone (S. Trinidad fault zone) and was highlighted by a $M_w$ 5.3 earthquake on 23 August 2011, the largest earthquake in the Basin's recorded history.
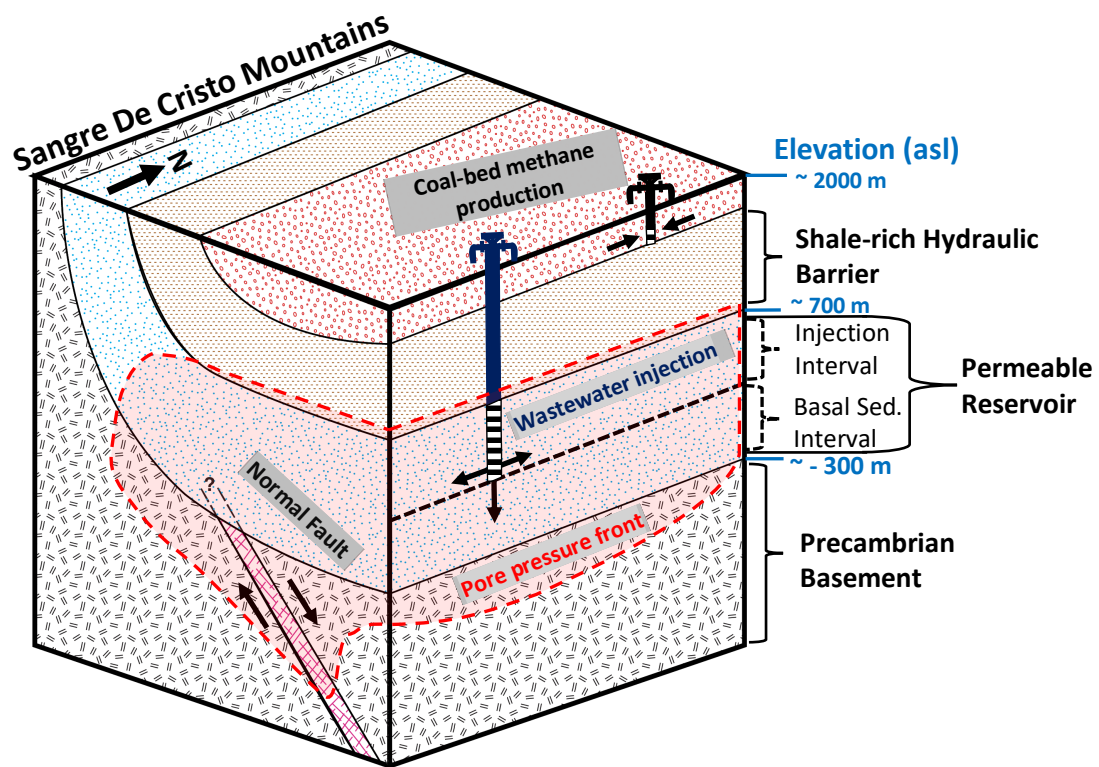


**Figure 2.** Schematic diagram showing the Raton Basin geologic architecture, industrial activities, hydrostratigraphic classifications and pore pressure front (red shade). The diagram conceptualizes a critically stressed normal fault hydraulically connected to the permeable reservoir being perturbed by wastewater injection conducted stratigraphically above the seismogenic zone.

Studies have attributed the Raton Basin's increase in seismicity to wastewater injection (Nakai et al., 2017b; Rubinstein et al., 2014); although a detailed analysis of seismicity from 2016 - 2020 indicates that earthquake – earthquake interaction may be more significant than pore pressure diffusion (Glasgow et al., 2021). Glasgow et al. (2021) suggested that earthquake sequences in the Raton Basin are initiated by anthropogenic perturbation from injection, but stored tectonic stress continues to drive the sequence through earthquake – earthquake interaction. The initiation of earthquake sequences from anthropogenic perturbation highlights the question: what is the relationship between pore pressure diffusion and early-stage induced seismicity?
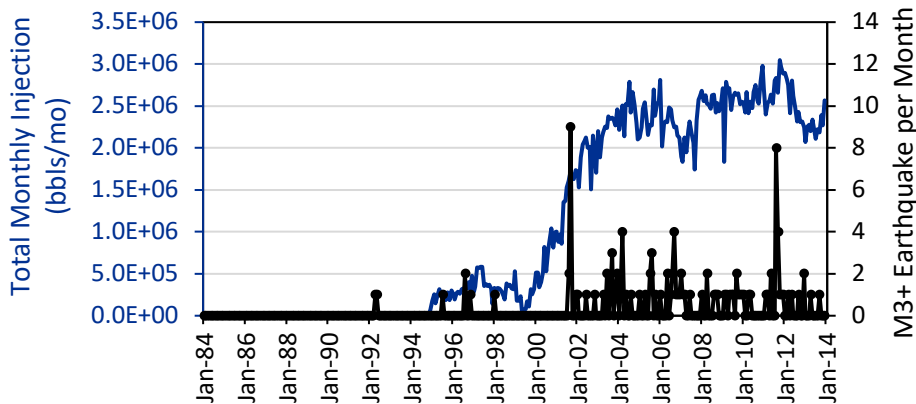


**Figure 3.** Comparison of total basin-wide monthly wastewater injection (blue line) and the number of M3+ earthquakes per month (black line) from the Rubinstein et al. (2014) catalog.

Nakai et al. (2017b) found that sufficient pore pressure perturbation on the Vermejo Park fault zone between 2008 and 2010 had accumulated in the seismogenic zone to induce seismicity. This study, however, only focused on one of the fault zones and did not investigate early-stage seismicity when pore pressure diffusion was likely the triggering mechanism before earthquake – earthquake interaction started. In this study we construct a numerical pore pressure model to determine a triggering threshold

of early-stage seismicity, with a particular emphasis put on the N. Trinidad fault zone and the August-September 2001 earthquake sequence. Our model takes into consideration additional geologic detail that the previous model did not, such as the elevation variations of the relevant hydrostratigraphy. From this model we look to characterize what pore pressure increase initiated induced seismicity in the Raton Basin in hopes that our findings can assist in preliminary assessments of future wastewater injection sites.

## 2. Methods

### 2.1 Injection and Seismicity Data

Monthly injection rates for the wells in Colorado and New Mexico (Table A-1) were collected from the Colorado Oil and Gas Conservation Commission (COGCC, 2020) and the New Mexico Oil Conservation Division (NMOCD, 2020), respectively. Injection between October 1999 and May 2006 was not reported for the New Mexico injection wells but water production was reported. Prior studies have shown that produced water from 1999 to 2006 can be used as a proxy for New Mexico's unreported injection (Nakai et al., 2017b; Rubinstein et al., 2014). We use the reported volume of produced water to estimate the approximate injection in New Mexico from 1999 to June 2006, additional information regarding how we specified injection can be found in Appendix A.

For this study we utilize two earthquake catalogs, the Rubinstein et al. (2014) catalog and the Nakai et al. (2017a) catalog. The Rubinstein et al. (2014) catalog contains earthquakes from 1963 to 2013 and incorporates the earthquakes recorded by

6

the USGS temporary seismic networks deployed between September 2001 – October 2001 and August 2011 – December 2011. Most of the catalog has a horizontal uncertainty of 15 km because of the low-density seismic network in the region, with the exception of the earthquakes recorded by the temporary seismic networks which have horizontal uncertainties of 2 km for the 2001 deployment and 0.3 km for the 2011 deployment (Rubinstein et al., 2014). The Nakai et al. (2017a) catalog contains seismicity from 2008 – 2010 when the EarthScope Transportable Array was in the region. This catalog provides more accurate seismicity locations but only recorded earthquakes between 2008 – 2010 at a time when induced seismicity was already well-established throughout much of the Basin.

## 2.2 Conceptual Model

## 2.2.1 Structure Maps

To create a realistic representation of the Basin's subsurface hydrogeologic architecture, we based our model's hydrostratigraphy off Geldon (1989) and developed structure maps of the bottom of the shale-rich hydraulic barrier and top of the Precambrian basement (Figure A-1). The structure maps were constructed using well lithology logs (COGCC, 2020; NMOCD, 2020; Tables A-2, A-3), geologic maps (Baldwin and Muehlberger, 1959; Clark and Read, 1972; Fridrich et al., 2012; Garrabrant,1993; Johnson, 1969; Johnson, 1974; Johnson , 1975; Lindsey, 1995a; Lindsey, 1995b; Lindsey, 1996; Pillmore, 2003; Vine, 1974; Wallace, 1996; Wanek, 1959) and Precambrian basement data (Hemborg, 1996). The stratigraphic data was interpolated using a natural neighbor algorithm to generate surfaces that encompasses the entire

model domain. We then inserted the structure maps into the numerical model to represent subsurface elevation variations.

## 2.2.2 Faults

There are three prominent seismic lineations in the Raton Basin: the Trinidad fault zone, Vermejo Park fault zone and Tercio fault zone (Figure 1). In the hydrogeologic model we incorporate all three fault zones and assign hydrogeologic parameters that are different from the unfaulted Precambrian basement. Other studies have suggested that the fault zones are constructed of many small faults of variable strike and dip (Glasgow et al., 2021; Rubinstein et al., 2014) but modeling the exact geometry of the faults is outside the scope of this research. We are mainly concerned with how the fault contributes to vertical pore pressure diffusion into the basement. For that reason, the seismic lineations are simplified into three continuous zones each around 250 m wide, which is within the range of plausibility for a mature fault damage zone width (e.g., Savage and Brodsky, 2011). The strike, dip and depth of the three fault zones were determined based on a combination of the earthquake catalogs, moment tensors and knowledge of the regional stress regime. The orientations of the fault zones agree with the normal faulting observed in the Basin and with the regional east-west extensional stress regime (Herrmann, 2020). Specifics regarding the geometry of the fault zones can be found in the Appendix A.

## 2.3 Governing Equation

A three-dimensional numerical pore pressure model was developed for a heterogenous, anisotropic domain using MODFLOW-2005, a modular finite difference code developed by the USGS (Harbaugh et al., 2005). The code numerically solves the

groundwater flow equation (1) to simulate pore pressure diffusion caused by wastewater injection:

$$\frac{\partial}{\partial x}\left(K_{xx}\frac{\partial h}{\partial x}\right) + \frac{\partial}{\partial y}\left(K_{yy}\frac{\partial h}{\partial y}\right) + \frac{\partial}{\partial z}\left(K_{zz}\frac{\partial h}{\partial z}\right) + \sum_{n=1}^{N} Q_n(t)\delta(x - x_n)(y - y_n)(z - z_n) = S_s\frac{\partial h}{\partial t} \qquad (1)$$

where $h$ is hydraulic head (m), $K_{xx}$, $K_{yy}$, $K_{zz}$ are the principle components of the hydraulic conductivity tensor (m/s), $S_s$ is specific storage (m$^{-1}$), $x,y,z$ are spatial coordinates, $t$ is time (s), $\delta$ is the Dirac delta function (m$^{-1}$), $Q_n$ is the injection rate for well $n$ and $N$ is the number of injection wells.  As input into the model, monthly injection rates and details regarding well construction (Table A-1) were extracted from the COGCC (2020) and NMOCD (2020) and combined with a range of hydraulic parameters (Table 1) that were collected from various sources discussed in more detail below.

**Table 1. Hydrostratigraphic Framework Hydraulic Diffusivities**

| Hydrostratigraphic unit | Homogeneous hydrostratigraphic framework diffusivities (m$^2$/s) | Heterogeneous hydrostratigraphic framework diffusivities (m$^2$/s) |
|---|---|---|
| Hydraulic Barrier | 10$^{-8}$ | 10$^{-8}$ |
| Injection Interval | 0.1 – 10 | 0.1 – 10 |
| Basal Sedimentary Interval | homogeneous permeable reservoir, no low-D basal sedimentary interval | 0.01 |
| Precambrian Basement | Depth decaying (Fig. 4a) | Depth decaying (Fig. 4a) |
| Fault Zones | 0.01 – 1.0 | 0.01 – 1.0 |

## 2.4 Hydrogeologic Parameters

Hydraulic diffusivity is a hydrogeologic parameter used to describe pressure diffusion in a saturated porous medium. Diffusivity is equal to the ratio of hydraulic conductivity to specific storage:

$$D = \frac{K}{S_s} \tag{2}$$

where $D$ is diffusivity (m²/s), $K$ is hydraulic conductivity (m/s) and $S_s$ is specific storage (m⁻¹). When expressing the components of hydraulic conductivity and specific storage into equation (2) it becomes apparent that diffusivity is a function of both medium and fluid properties (3) (Fetter, 2018):

$$D = \frac{k}{\mu(\alpha + n\beta)} \tag{3}$$

where $k$ is permeability (m²), $\mu$ is dynamic viscosity (Pa·s), $n$ is porosity (dimensionless), $\alpha$ and $\beta$ are rock and fluid compressibility (Pa⁻¹), respectively. Given the dependence of both medium and fluid properties, this study takes into consideration both pressure and temperature gradients.

**2.4.1 Fluid Properties**

Fluid composition and the effects of pressure and temperature on fluid viscosity are often not considered in modeling studies. The total dissolved solids (TDS) concentration of injection brine, if sufficiently larger than the TDS of the in-situ basement fluid, can cause density-driven flow of injection brine into the basement. The advection of injection brine results in increased pore pressure in the seismogenic zone even after injection has stopped (Pollyea et al., 2019, 2020). Additionally, fluid viscosity can change over an order of magnitude due to increased temperature over a large depth range, thus effecting the diffusivity of the medium.

Produced water from the Raton Basin has a relatively low TDS (~ 2800 ppm) and likely is not sufficient to produced density-driven brine flow (Blondes et al., 2018). The low TDS means transport of injection fluids is not enhanced by density variations

between the injection fluid and the in-situ fluid making the pore pressure perturbation in the Raton Basin dominated by wellhead diffusion; therefore, we do not model the effects of fluid TDS. To incorporate the effects of increased pressure and temperature on diffusivity, we use a hydrostatic pressure gradient and geothermal gradient of 25°C/km to solve for fluid viscosity. Additional information can be found in Appendix A.

**2.4.2 Hydrostratigraphic Frameworks and Hydrogeologic Data**

For much of the Basin's deep hydrostratigraphy, there is minimal locally recorded hydraulic conductivity and specific storage measurements that can be used to solve for diffusivity. To produce a range of diffusivities, the available data from the Raton Basin was coupled with hydrogeologic data from basins with similar hydrostratigraphy. The diffusivities were combined into two hydrostratigraphic frameworks, one with a homogeneous permeable reservoir and another with a heterogeneous permeable reservoir (Table. 1). The homogeneous framework assumes the permeable reservoir is homogeneous with hydrogeologic properties representative of the injection interval. The heterogeneous framework divides the permeable reservoir into the injection interval and basal sedimentary interval (Figure 2). The spatial coverage, thickness and hydrogeologic properties of the basal sedimentary interval (Pennsylvanian and older) is uncertain. In the Raton Basin, the Permian-Pennsylvania Sangre de Cristo formation has been reported to unconformably overlay the Precambrian basement (Robinson et al., 1964). Cores taken from the Sangre de Cristo Formation suggest permeabilities between $10^{-16} - 10^{-15}$ m$^2$ (Bohlen, 2013), which would result in temperature and pressure adjusted diffusivities around $0.001 - 0.01$ m$^2$/s. The heterogenous framework used the same injection interval diffusivities as the homogeneous framework but

11

assigned the basal sedimentary interval, approximately 500 m thick, a diffusivity of 0.01 $m^2$/s (Table 1).

A shale-rich hydraulic barrier overlies the injection interval (Figure 2) and consists of the Pierre Shale, Niobrara Formation and Benton Formation. The hydraulic barrier was simplified into a single unit with hydrogeologic characteristics representative of the Pierre Shale. The hydraulic barrier was assigned a diffusivity of $10^{-8}$ $m^2$/s in all model simulations based on parameters derived from a field scale osmosis study (Garavito et al., 2006) and adjusted for a temperature and pressure of approximately 50°C and 18 MPa, respectively.

The injection interval consists of multiple geologic units that are simplified into a single hydrostratigraphic unit. A single injection recovery step rate test conducted in the Raton Basin backed out permeabilities for the Dakota formation and Entrada Sandstone (upper portion of the injection interval) ranging from 5.8 x $10^{-14}$ – 8.9 x $10^{-14}$ $m^2$ (Hernandez and Weingarten, 2019). To further determine a range of hydrogeologic parameters for the injection interval, we utilized additional data from hydrologic field testing, lab-based core analyses and calibrated models from proxy locations (Bredehoeft et al., 1983; Gries et al., 1976; Teeple et al., 2021). Permeabilities for the Dakota formation derived from proxy locations are similar to those measured in the Raton Basin. The hydraulic conductivities, when adjusted for a temperature and pressures corresponding to the depth of the injection interval (70°C and 25 MPa), are 1.4 x $10^{-6}$ – 2.1 x $10^{-6}$ m/s. The corresponding diffusivities, when using the average specific storage from proxy locations ($\sim$ 1 x $10^{-6}$ $m^{-1}$), are 1.4 – 2.1 $m^2$/s. Given

uncertainties associated with determining hydraulic conductivity and specific storage, we use a range of diffusivities for the injection interval between 0.1 – 10 m²/s (Table 1).
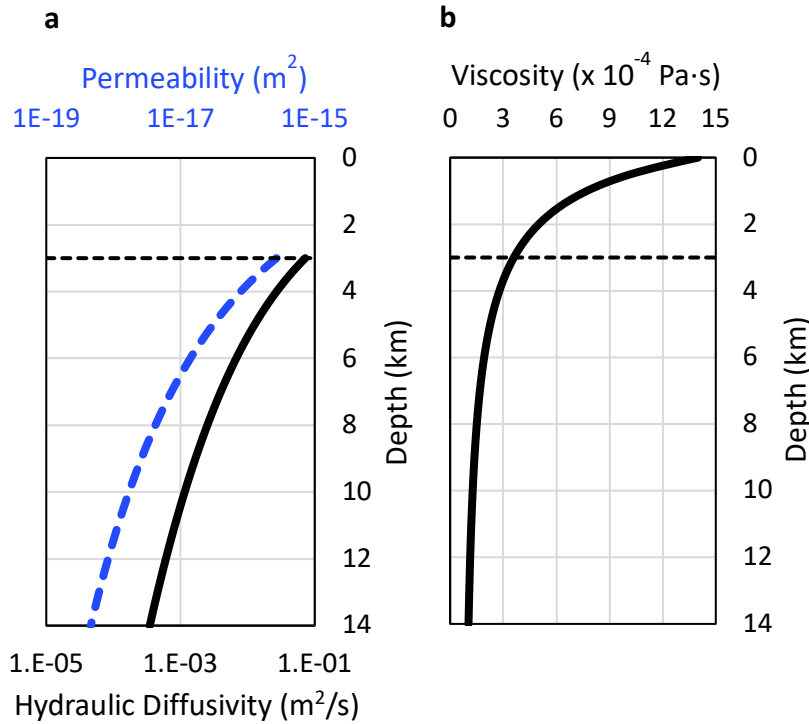


**Figure 4**. Vertical profiles showing the basement's depth decaying (a) permeability in blue (dashed), hydraulic diffusivity ($S_s$ 1x10$^{-7}$ 1/m) in black (solid) and (b) fluid viscosity. The dashed horizontal line represents the top of the basement.

Directly measured hydrogeologic properties of Precambrian basement are scarce, but basement permeability has been shown to decrease as a function of depth causing significant heterogeneity over large depth ranges (Kuang and Jiao, 2014; Manning and Ingebritsen, 1999; Saar and Manga, 2004). To represent the basement's heterogeneous diffusivity, we took into consideration depth dependent viscosity (Huber et al., 2009; Wagner and Pruß, 2002) and used a depth decaying permeability function equation (4) from Kuang and Jiao (2014):

$$\log k = \log k_r + (\log k_s - \log k_r)(1 + z)^{-\alpha} \tag{4}$$

where $k$ is permeability (m$^2$), $k_r$ is the residual permeability at depth (m$^2$), $k_s$ is the

permeability at zero depth (m$^2$), $z$ is the depth (km) and $\alpha$ is the decay index

(dimensionless). As seen in Figure 4, the basement's diffusivity decays with depth from

~ 0.07 m$^2$/s at the top of the basement (~ 3 km deep) to ~ 0.007 m$^2$/s when 3 km below

the basement top (~ 6 km deep).

Within the basement we modeled three fault zones that are hydraulically

connected to the permeable reservoir. The three faults were assigned bulk diffusivities

that ranged from 0.01 – 1 m$^2$/s to simulate a range of fault characteristics from a low

diffusivity sealing fault to a high diffusivity conductive fault. The range of diffusivities was

established based on data collected from a tidal response study (Xue et al., 2013), lab-

based core analyses of fault gouge and damage zone (Ree et al., 2018) and values

used in similar hydro-mechanical models (Goebel et al., 2017; Nakai et al., 2017b; Yeo

et al., 2020; Zhang et al., 2013).

## 2.5 Model Discretization and Boundary Conditions

The model domain dimensions are 130 km x 200 km x 11-14 km (depth) (Figure

A-2). The domain was discretized into approximately 5.5 million cells with horizontal

discretization being 250 m x 250 m in the injection and faulted regions and 1 km x 1 km

cells in the outer reaches of the model. The model was vertically discretized into 53

layers of varying thickness to accommodate fluctuating topography of lithological units.

The hydraulic barrier was discretized into 6 layers with layer thickness decreasing with

depth. The permeable reservoir was discretized into 12 layers with an average

thickness of ~ 100 m. The basement was divided into 35 layers with an average

thickness of ~ 250 m. The size of the model domain was designed to minimize

boundary effects on the no flow boundary conditions assigned to the lateral and bottom boundaries of the model. The top of the model domain was made an open boundary.

# 3. Results

A numerical pore pressure model was developed to investigate the relationship between wastewater injection and increased seismicity. Two hydrostratigraphic frameworks were developed to represent the Raton Basin's subsurface hydrogeologic architecture, one with a homogeneous permeable reservoir and another with a heterogeneous permeable reservoir with the basal sedimentary interval being assign a low diffusivity of 0.01 m$^2$/s. Model simulations were run on both frameworks for a range of diffusivities for the injection interval and fault zones (Table 1). Based on the data discussed in Methods,

the heterogeneous permeable reservoir was the most reasonable representation of the Basins subsurface hydrogeologic architecture. In the following subsections we present modeled pore pressure increases from the heterogeneous model framework to investigate the spatiotemporal relationship between pore pressure diffusion, early-stage seismicity, and high-rate injection wells. We include model results from all scenarios except those generated using an injection interval diffusivity of 0.1 m$^2$/s because it produced unreasonably high pore pressure increases at the well that do not agree with underpressure estimates and wellhead pressures or lack thereof. More information regarding parameter constraining can be found in Appendix C.

## 3.1 N. Trinidad Fault Zone: Seismicity, Pore Pressure and Injection

The August – September 2001 earthquake sequence marked the first occurrence of induced seismicity within the Raton Basin. The earthquakes sequence occurred along the northern portion of the Trinidad fault zone (N. Trinidad fault zone), a fault zone that was previously quiescent (Figure 5a). The earthquake sequence included 11 M3+



**Figure 5.** Modeled pore pressure change on each fault zone, located at white dots in Figure 5a, compared to monthly earthquakes within 15 km of the fault zone from the Rubinstein et al. (2014) catalog. Vertical black lines denote when a significant injection well became active and vertical translucent blue strips signifies when the USGS temporary seismic networks were active. (a) Modeled pore pressure at 3 km deep at a single location on the N. Trinidad fault zone. (b) Modeled pore pressure at 4 km deep at a single location on the Vermejo Park fault zone. (c) Modeled pore pressure at 5 km deep at a single location on the Tercio fault zone.

earthquakes between 28 August 2001 and 21 September 2001. The temporary seismic

network recorded additional earthquakes in September and October but the

earthquakes were either < M3 or did not have a magnitude calculated. Most of the

seismicity associated with the 2001 sequence occurred around 3 km deep near the

sedimentary-basement interface (Meremonte et al., 2002; Rubinstein et al., 2014).

Modeled pore pressure increases at 3 km deep, as of 1 September 2001, ranged

between 0.007 – 0.03 MPa (Figures 5a, 6a, 6b). When projecting seismicity from

September 2001 onto a cross section of pore pressure diffusion all the seismicity falls

within an area of pore pressure increase of 0.01 MPa or greater when modeling with an

injection interval diffusivity of 1.0 m$^2$/s, regardless of fault zone diffusivity (Figure B-1).
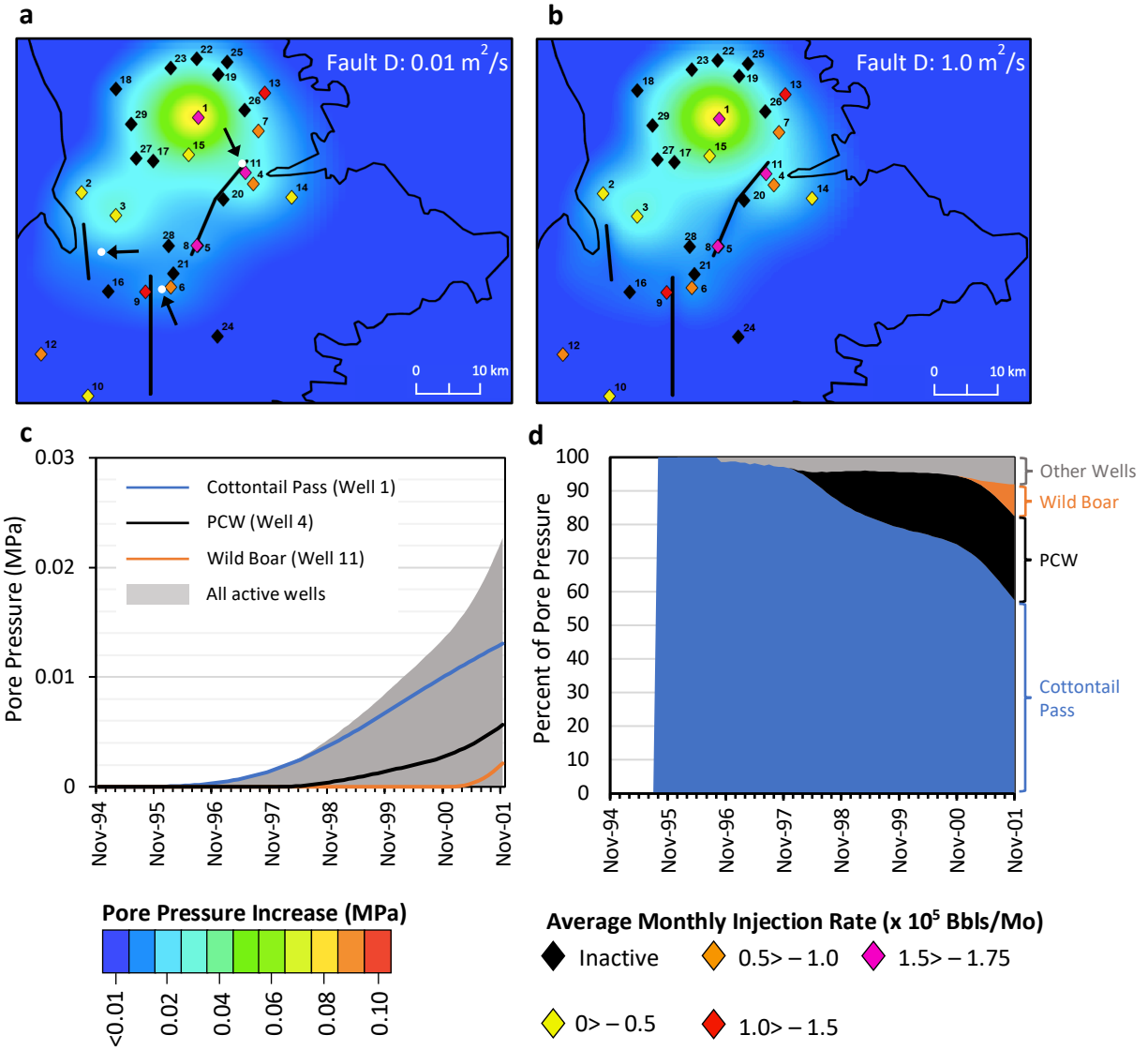
**Figure 6. (**a, b) Map view of modeled pore pressure perturbation at 3 km deep as of 1 September 2001 when using an injection interval diffusivity of 1.0 m²/s with a (a) sealing fault zone or a (b) conductive fault zone. The diamonds represent the locations of the injection wells with colors corresponding to the average injection rate of the wells prior to September 2001 and labeled with the wells age number (1 = oldest well). The location of the fault zones at the top of the basement are denoted by the black lines. (c, d) Contribution to pore pressure change on the N. Trinidad fault zone at 3 km deep as of 1 September 2001 from the Cottontail Pass well (blue), PCW well (black) and the Wild Boar well (orange). (c) Comparison of total pore pressure change from all active wells (gray) to pore pressure change caused by the three individual wells. (d) Percent that the three wells contributed to total pore pressure change generated by all active wells.

Pore pressure perturbation on the N. Trinidad fault zone was negligible until early 1998, after which pore pressure continued to rise at an increasing rate as additional injection wells started becoming active (Figure 5a). Early perturbation on the N. Trinidad Fault was caused by the Cottontail Pass injection well (well 1), located just over 10 km northwest of the fault zone (Figures 5a, 6a – c). The Cottontail Pass injection well started injecting in November 1994 and had the second highest average monthly injection rate prior to the August- September 2001 earthquake sequence (Figure B-2; Table B-1). The highest rate injection well at this time was the Wild Boar injection well (well 11), located within a kilometer of the N. Trinidad fault zone (Figures 6a, b-2; Table B-1). The well began injecting in August 2000 but pore pressure perturbation caused by the well was not observed in the fault zone until mid 2001 (Figure 6c). Additional perturbation on the fault zone was caused by the PCW well (Well 4), located approximately 2.5 km southeast of the fault zone (Figure 6a). The PCW well became active in July 1997 and injected at low to moderate rates until March 2001 when it started injecting at higher rates (Figure B-2; Table B-1).

## 3.2 Vermejo Park Fault Zone: Pore Pressure, Seismicity and Injection

The Vermejo Park fault zone is located just south of the Colorado-New Mexico border in the center of the Basin (Figure 1). Seismicity started to migrate into this portion of the Basin as early as December 2001 and has remained highly active (Figure 5b). Within a 15 km radius of the northern extent of the fault zone, 16 earthquakes were recorded before the August-September 2005 earthquake sequence, 14 of which were M3+. The exact location and depth of early-stage seismicity in this portion of the Basin

is uncertain because of the low-density seismic network. Additionally, injection rates for the New Mexico wells had to be estimated because operators in New Mexico did not start reporting injection rates until June 2006. The uncertainty of the seismicity and injection data makes correlating pore pressure and early-stage seismicity more ambiguous than on the N. Trinidad fault zone.

The catalog from Nakai et al. (2017a), which contains seismicity from 2008 to 2010, indicates that there are high concentrations of earthquakes on the Vermejo Park fault zone between 3 and 10 km deep with an average depth between 4 and 5 km, this is corroborated by nearby moment tensors from Herrmann (2020). Modeled pore pressure at the Vermejo Park fault zone was continuously monitored at 3 km deep (top of the fault zone) and 4 km deep. As of December 2001 and August 2005, pore pressure increase at 3 km deep ranged between 0.005 – 0.02 MPa and 0.03 – 0.2 MPa, respectively (Figure B-3). At 4 km deep, as of December 2001 and August 2005, pore pressure increase ranged between 0 – 0.004 MPa and 0.003 – 0.04 MPa, respectively (Figure 5b).

Modeled pore pressure first became elevated on the northern portion of the fault zone, where most of the injection wells are located (Figures 6a, 6b). Pore pressure on the northern extent of the fault zone increased gradually until early 2001 when pore pressure started to increase at an elevated rate (Figures 5b, B-2). The initial pore pressure perturbation was likely caused by the Apache 10-3 (well 2) and Apache 19-10 (well 3) but these wells were not high-rate injectors; so the initial perturbation was small (Figures 5b, B-2). When pore pressure started increasing at an elevated rate multiple high-rate injectors had been injecting for at least 8 months (Figures 5b, B-2). The

closest wells are VPR 042 (well 9) and VPR 007 (well 6), located 0.6 km and 3 km from

the northern extent of the fault zone, respectively (Figure 6a). Both wells are estimated

to have injected at moderately high to high rates and likely accounted for much of the

perturbation on the fault zone (Figures 5b, B-2; Table B-1). Two additional high-rate

injectors, VPR 39 (well 8) and VPR 99 (well 16), also contributed to pore pressure

perturbation but are located 9 km and 6.5 km from the fault zone, respectively (Figure

6a).

## 3.3 Tercio Fault Zone: Pore Pressure, Seismicity, and Injection

The Tercio fault zone is located on the Colorado-New Mexico border on the

western side of the Basin (Figure 1). Seismicity started to occur within 15 km of the fault

zone as early as June 2003 (Figure 5c). The Nakai et al. (2017a) catalog indicates that

there are high concentrations of earthquakes between 3 and 7 km, while nearby

moment tensors from Herrmann (2020) predominantly range in depth between 3 and 5

km. Modeled pore pressure at the Tercio fault zone was continuously monitored at

approximately 3 km (top of fault zone) and 5 km deep. As of June 2003, modeled pore

pressure at 3 km deep ranged between 0.007 – 0.02 MPa (Figure B-3). At 5 km deep,

as of June 2003, modeled pore pressure increase ranged between 0 – 0.005 MPa

(Figure 5c).

Pore pressure gradually increased on the Tercio fault zone until mid 2003 when

pore pressure started to increase at an elevated rate (Figure 5c, B-2). The initial

perturbation was likely caused by wells Apache 10-3 (well 2) and Apache 19-10 (well 3).

Both wells are within 5 km of the fault zone but have predominantly injected at low rates

(Figure 6a, B-2). As additional high-rate injection wells (VPR 007 (well 6), VPR 042 (well

9), VPR 99 (well 16) and VPR 39 (well 8)) started injecting the rate of pore pressure change increased (Figure 5c, B-2). The two closest high-rate injectors are VPR 99 and VPR 042, located 4 km and 9 km from the fault zone, respectively (Figure 6a). Unlike the other two fault zones, the Tercio fault zone is located farther away from high-rate injectors so there is a larger lag time between the start of injection and the expression of perturbation in the fault zone.

# 4. Discussion

## 4.1 N. Trinidad Fault Zone: August – September 2001 Earthquake Sequence

The August – September 2001 earthquake sequence represents the onset of induced seismicity in the Raton Basin with a M3.4 earthquake on 28 August 2001. Earthquake sequences in the Raton Basin have been characterized by initial earthquakes being triggered by anthropogenic perturbation while subsequent earthquakes are the result of stored tectonic stress and earthquake – earthquake interactions (Glasgow et al., 2021). The 28 August 2001 earthquake was likely triggered by pore pressure diffusion from nearby injection wells. Modeled pore pressure change at this time ranged between 0.007 – 0.03 MPa. When constraining modeled pore pressure to the scenarios that only used an injection interval diffusivity of 1.0 $m^2$/s, which is the diffusivity closest to that estimated for the Basin's injection formations, modeled pore pressure ranges from 0.02 – 0.03 MPa. This range of pore pressure increase is in agreement with previously suggested triggering thresholds for induced

seismicity in other regions (e.g. Keranen et al., 2014; Hornbach et al., 2015; Ogwari et al., 2018).

Prior to the 2001 earthquake sequence, 15 wells had been injecting in the Raton Basin. Three of the injection wells are responsible for 92% of the pore pressure accumulation on the N. Trinidad fault zone as of 1 September 2001 (Figure 6d). The three wells include the Cottontail Pass (well 1), PCW (well 4) and Wild Boar (well 11). The Wild Boar well had the highest average injection rate at the time (Table B-1) and is located within a kilometer of the fault zone. It was previously suggested to be the most significant well in inducing the 2001 earthquake sequence (Rubinstein et al., 2014) but our model indicates that it accounted for only 7% of pore pressure increase on the N. Trinidad fault zone as of 1 September 2001 (Figure 6d). The PCW well, located ~ 2.5 km southeast of the fault zone, accounted for 24% of the pore pressure increase. The Cottontail Pass well, located ~10 km northwest of the fault zone, is responsible for 61% of the pore pressure perturbation.

The high injection rate and proximity of the Wild Boar well to the N. Trinidad fault zone made it an obvious well to attribute blame for triggering the 2001 earthquakes sequence, but what was not considered before was the hydrogeology of the Basin. The basal sedimentary interval has a moderately low permeability (Bohlen, 2013) which restricts pore pressure diffusion into the basement and creates a lag time between the start of injection and expression of perturbation in the basement. Additionally, the Wild Boar well had only been injecting for one year, whereas the PCW well had been injecting for over four years and the Cottontail Pass well had been injecting for just under seven years (Figure 5a). The combination of the low permeability basal

sedimentary interval and the short duration of injection limited the Wild Boar wells

contribution to pore pressure perturbation on the N. Trinidad fault zone. From this

analysis, the most significant well in inducing the 2001 earthquake sequence was likely

the Cottontail Pass well. This becomes interesting when considering the average

injection rate of the Cottontail Pass well (~ 166,000 bbls/mo; Table B-1) is well below

the average rate of some high-rate injection wells (300,000 + bbls/mo) in other regions,

such as Oklahoma (e.g., Keranen et al., 2014; Goebel et al., 2017). This highlights that

wells injecting at moderate rates over time can contribute significant enough pore

pressure perturbation to induced seismicity on critically stressed faults even if it is not in

close proximity.

## 4.2 Vermejo Park and Tercio Fault Zones

Given the data we have, the exact timing of early-stage seismicity is unknown

based on earthquake catalogs alone. As an alternative we assumed the pore pressure

triggering threshold for early-stage seismicity on the Vermejo and Tercio fault zones are

similar to the triggering threshold established for the August-September 2001

earthquake sequence. This is a reasonable assumption because the fault zones are

thought to be composed of many fault segments of varying strike (Glasgow et al., 2021),

meaning all three fault zones likely have fault segments that are optimally oriented and

require similar amounts of perturbation for failure. In the following we compare

seismicity to the timing in which the Vermejo Park and Tercio fault zones reached 0.02

MPa of pore pressure change when modeling an injection interval diffusivity of 1.0 $m^2$/s.

At the average depth on seismicity (~ 4 km), the Vermejo Park fault zone

reached 0.02 MPa of pore pressure increase on February 2004, April 2005 and July

2007 (Figure 5b). The timing was dependent on the fault zone diffusivity, with the earliest time corresponding with a conductive fault zone (1.0 $m^2$/s) and the latest time corresponding with a sealing fault zone (0.01 $m^2$/s). Prior to February 2004, April 2005 and July 2007, the Rubinstein et al. (2014) catalog recorded 9 earthquakes, 15 earthquakes and 36 earthquakes within the 15 km of the fault zone, respectively. Additionally, the scenario that used a sealing fault zone did not surpass 0.02 MPa or pore pressure increase until after the August-September 2005 earthquake sequence. This sequence is considered to be the latest possible time that represents early-stage seismicity on the Vermejo Park fault zone.

At the average depth of seismicity (~ 5 km), the Tercio fault zone reached 0.02 MPa of pore pressure increase on January 2007, July 2010 and September 2015. Like the Vermejo Park fault zone the timing was dependent on fault zone diffusivity. Prior to January 2007 and July 2010, the Rubinstein et al. (2014) catalog recorded 17 earthquakes and 39 earthquakes within 15 km of the fault zone, respectively. Even more earthquakes were recorded before September 2015, but the Rubinstein catalog only includes earthquakes through 2013. The Nakai et al. (2017a) catalog first recorded seismicity on the Tercio fault zone on 17 July 2008, well before the intermediate diffusivity and sealing fault zones reached 0.02 MPa of pore pressure increase.

Both fault zones reached 0.02 MPa of pore pressure increase years after seismicity started being recorded within 15 km of the fault zones. It seems unlikely that even the earliest time in which 0.02 MPa of pore pressure increase was reached represents the timing of early-stage seismicity on either fault zone. This may indicate that early-stage seismicity occurred at shallower depths, closer to the sedimentary-
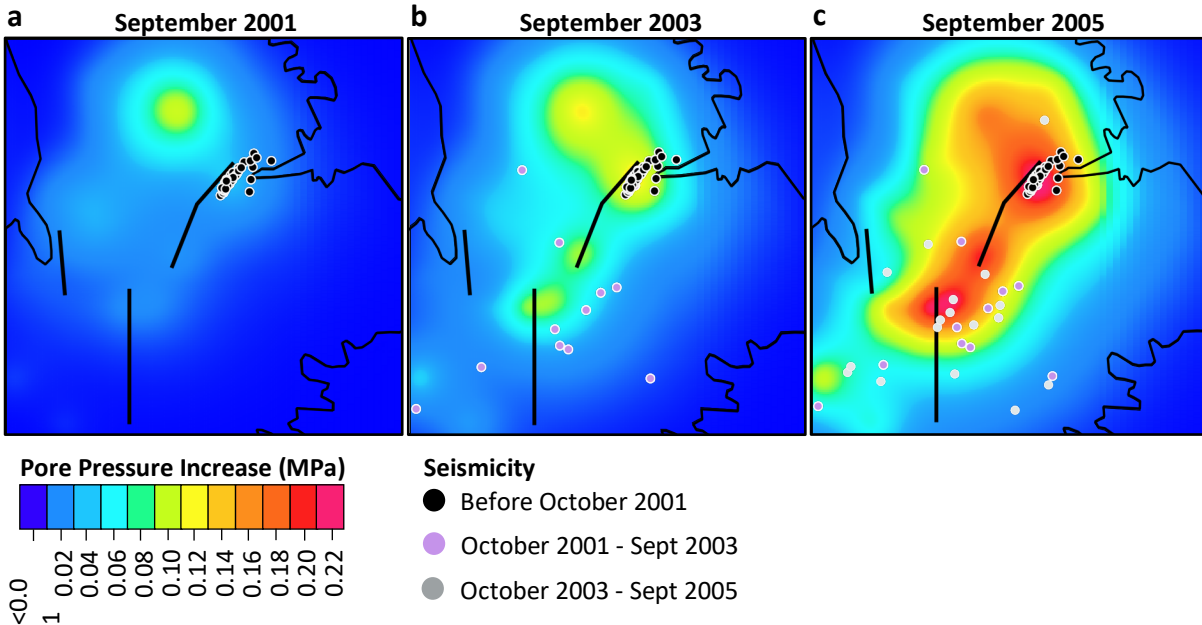
**Figure 7.** Pore pressure perturbation at the top of the basement (3 km deep) when modeling an injection interval diffusivity of 1.0 $m^2$/s and a sealing fault (0.01 $m^2$/s), the black lines represent the location of the fault zone at the top of the basement. (a) Pore pressure change as of September 2001 with seismicity recorded before October 2001 (black circles) projected onto the map of modeled pore pressure. (b) Pore pressure change as of September 2003 with seismicity recorded before October 2003 (purple circles) projected onto the map of modeled pore pressure. (c) Pore pressure change as of September 2005 with seismicity recorded before October 2005 (gray circles) projected onto the map of modeled pore pressure.

basement interface. It also could be the result of local hydrogeologic heterogeneity that was not represented in the model, such as a fault zone that penetrates the basal sedimentary interval. Additionally, the injection rates for New Mexico wells are an estimate, because operators were not required to report injection rates until May 2006. This accumulation of unknowns prohibits us from precisely deducing the date of early-stage seismicity on the Vermejo Park and Tercio fault zones. On a broader scale, the spatiotemporal occurrence of seismicity is in agreement with modeled pore pressure diffusion. Seismicity first occurred on the N. Trinidad fault zone followed by the Vermejo Park fault zone and lastly the Tercio fault zone. Modeled pore pressure diffusion follows

the same pattern, first becoming elevated on the N. Trinidad fault zone followed by the Vermejo Park and later the Tercio fault zone (Figure 7).

## 4.4 Sensitivity Analysis

Pore pressure modeling is known to be sensitive to hydrogeologic properties. In many cases, hydrogeologic properties of a Basin's deep hydrostratigraphy are relatively unconstrained. The lack of in-situ pressure measurements limits our ability to calibrate these properties; it therefore is important to run sensitivity analyses to better understand how the modeled pore pressures may change with different hydrogeologic property scenarios. In the following we use the homogeneous hydrostratigraphic framework (Table 1), to examine how pore pressure perturbation changes when varying the diffusivity of the injection interval, fault zones and Precambrian basement.

### 4.4.1 Injection Interval Diffusivity vs Fault Zone Diffusivity

The diffusivity of the injection interval and fault zones are crucial factors when modeling pore pressure diffusion into critically stressed faults. To evaluate the model's sensitivity to these parameters, we calculated the coefficient of variation (Brown, 1998) for modeled pore pressure over a range of injection interval diffusivities (0.1 – 10 $m^2$/s) and fault zone diffusivities (0.01 – 1.0 $m^2$/s). The Coefficient of Variation (CV) is defined by CV = $\sigma$ / $\mu$, where $\sigma$ is standard deviation and $\mu$ is mean of modeled pore pressure. It is a measure of modeled pore pressure variability; the higher the CV the more sensitive the model is to the varied diffusivity. We calculated CV for two situations, (1) varying injection interval diffusivity but a constant fault zone diffusivity (Figure 8a, Table D-1) (2) varying fault zone diffusivity but a constant injection interval diffusivity (Figure 8b, Table D-1). We used monthly modeled pore pressure within the fault zone to calculate a

monthly CV (CV time series) for each scenario at 3 km, 4.5 km and 6 km deep (Figure D-1; Table D-1). The CV time series were averaged to create a single CV value for each scenario at each depth (Figure 8). The number of months used to calculate the average CV was the same for all scenarios but the starting and ending times used were different. This is because the pore pressure front reached the monitoring depths at different times (Figure D-1) and we wanted to make sure the same amount of time was used to calculate the average CV for all scenarios. For example, we calculated a CV per month at 3 km deep using four model simulations, all of which used a 1.0 $m^2$/s diffusivity fault zone but used different injection interval diffusivity (10 $m^2$/s, 5 $m^2$/s, 1 $m^2$/s, 0.1 $m^2$/s). The CV time series were averaged from December 1994 to August 2016 and represents modeled pore pressure variability at 3 km deep when varying the injection interval diffusivity with a constant 1.0 $m^2$/s fault zone diffusivity (Figure 8a, left most blue bar).
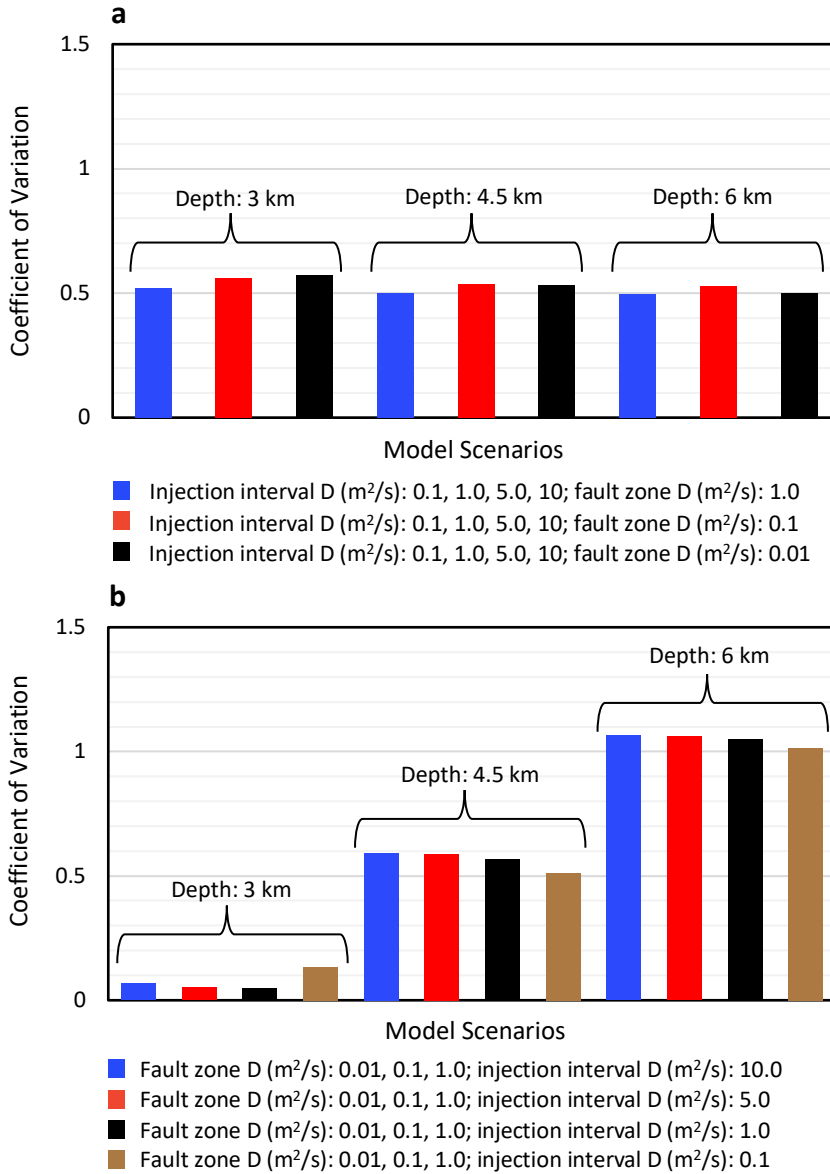
**Figure 8.** Coefficient of variation (CV, dimensionless) showing the pore pressure models sensitivity to varying the diffusivity of the injection interval and fault zones. The CV was calculated using modeled pore pressure for every month at 3 km, 4.5 km and 6 km deep which was then averaged to produce a single value for each model scenario. (a) CV when varying injection interval diffusivity and keeping the fault zone diffusivity constant. (b) CV when varying the fault zone diffusivity but keeping the injection interval diffusivity constant.

When varying the injection interval diffusivity with a constant fault zone diffusivity, CV only ranges between 0.49 – 0.57 (Figure 8a). When varying the fault zone diffusivity with a constant injection interval diffusivity, CV ranges between 0.05 – 1.06 (Figure 8b). The variable fault zone diffusivity situation led to a much wider range of CV and displays a depth trend with the highest CV at 6 km deep and the lowest CV at the 3 km depth (Figure 8b). Based on our analysis, fault zone diffusivity becomes more influential with increased depth into the basement and may become the governing parameter at several kilometers below the top of the basement. At an intermediate depth, pore pressure diffusion is significantly affected by both parameters. Near the sedimentary-basement interface, pore pressure diffusion is highly dependent on injection interval diffusivity with minimal dependence on fault zone diffusivity. When modeling pore pressure diffusion into basement, the hydrogeologic properties of both the injection interval and fault zones should be carefully considered.

## 4.4.2 Hydrogeologic Architecture of the Basement

The hydraulic properties of the basement are highly dependent on lithology and deformation history, but it is commonly cited that permeability of the basement decays with depth (Kuang and Jiao, 2014; Manning and Ingebritsen, 1999; Saar and Manga, 2004; Stober and Bucher, 2007; Stober, 2011). Stober and Bucher (2007) found that the crystalline basement, to several kilometers deep, has a hydraulic conductivity that averages around $10^{-8 \pm 1}$ m/s (permeability ~ 5 x $10^{-16 \pm 1}$ m$^2$). The corresponding diffusivity (assuming $S_s$ ~ $10^{-7}$ m$^{-1}$) is ~ 0.1 m$^2$/s.

Some hydro-mechanical studies choose to represent the basement as a homogeneous low diffusivity body (D $\leqq$ 0.0001 m$^2$/s) (e.g., Fan et al., 2019; Norbeck

and Horne, 2018; Tung et al., 2020; Zhai et al., 2019). Other studies, like this one, use a depth decaying permeability function to represent a basement that has a depth decaying diffusivity (e.g., Nakai et al., 2017b; Pollyea et al., 2019, 2020). The contrasting hydrogeologic representations of the basement raises the question what effect does basement diffusivity have on pore pressure diffusion into critically stressed faults? In the following, we compare the magnitude of modeled pore pressure change in a basement fault when using a homogeneous low diffusivity basement in contrast to a depth decaying diffusivity basement. The low diffusivity basement uses a homogeneous diffusivity of 0.0001 $m^2$/s while the depth decaying uses a diffusivity that decays from 0.07 $m^2$/s at the top of the basement to 0.0003 $m^2$/s at the bottom (Figure 4).

A homogeneous low diffusivity basement impedes vertical pore pressure diffusion into the unfaulted sections of the basement (Figure 9). The lack of vertical diffusion causes increased pore pressure perturbation in the sedimentary rock while also promoting lateral diffusion along the sedimentary-basement interface until reaching a fault zone which acts like a conduit for vertical pore pressure diffusion into the seismogenic zone (Figure 9). This allows for greater pore pressure build up along the entirety of the fault zones in all hydrogeologic scenarios with a conductive and intermediate diffusivity fault zone (Figure D-2). When modeled with a sealing fault, the shallow portion of the fault zone (3 km deep) still experiences more pore pressure build up with the low diffusivity basement, but at intermediate and deep depths (4.5 and 6 km) the difference in pore pressure increase between the two basement types is relatively small (Figures 9, D-2). This likely occurs because the low diffusivity basement primarily diffuses pore pressure into the top of the fault zone making pore pressure diffusion into

deeper parts of the fault zone highly dependent on fault zone diffusivity. In contrast, the

depth decaying basement allows pore pressure to diffuse into the unfaulted sections of

the basement which allows pore pressure to diffuse into the fault zone from within the

basement. This makes pore pressure perturbation at the intermediate and deeper

depths less dependent on fault zone diffusivity when modeling a depth decaying

basement.
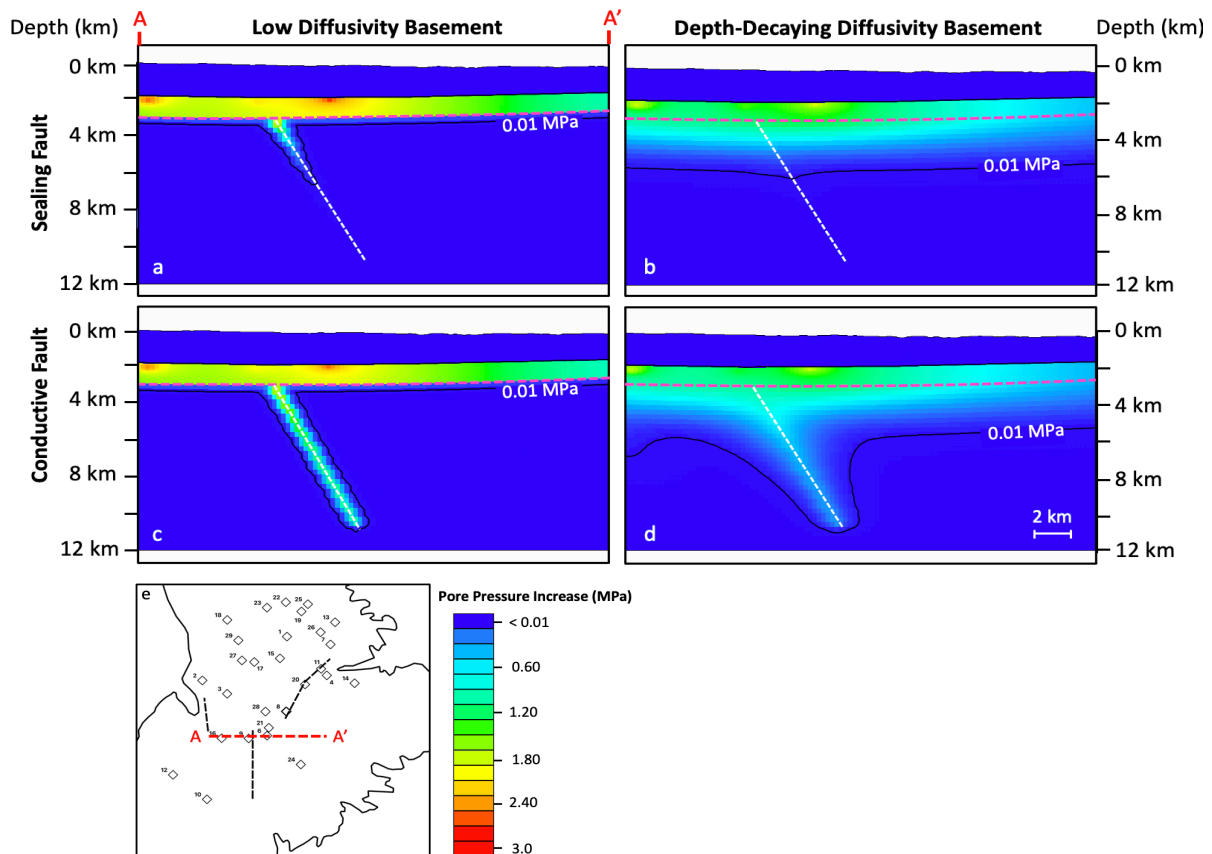


**Figure 9.** Comparison of pore pressure propagation into the basement when modeling a (a, c) homogeneous low diffusivity basement (D: 0.0001 $m^2$/s) and a (b, d) decaying diffusivity basement. An injection interval diffusivity of 1.0 $m^2$/s was used for all four plots, plots a and b used a sealing fault (D: 0.01 $m^2$/s) and plots c and d used a conductive fault (D: 1.0 $m^2$/s). The solid black line is a contour line of 0.01 MPa of pore pressure increase, the pink dashed line denotes the top of the basement and the white dashed line is the approximate centerline of the fault zone. (e) Map view showing the A – A' cross section location, faults (black dashed) and injection wells (diamonds).

Our analysis indicates that pore pressure diffusion into basement faults is

substantially affected by basement diffusivity. In some scenarios the low diffusivity

basement nearly tripled the amount of pore pressure increase that was produced by the depth decaying basement (Figure D-2). Additionally, the low diffusivity basement primarily diffused pore pressure into the top of the fault zone regardless of fault zone diffusivity while the depth decaying basement allows for pore pressure to diffusion into the top of the fault zone and from within the basement. Given the sensitivity to basement diffusivity, future modeling should carefully consider the hydrogeologic properties of the basement.

## 5. Conclusions

Over the last several decades the Raton Basin has experienced a significant increase is seismicity that corresponded with an increase in wastewater injection. The recent seismicity has been concentrated on the Trinidad fault zone, Vermejo Park fault zone and Tercio fault zone. A numerical pore pressure model was used to relate pore pressure diffusion to onset of seismicity on these fault zones. We draw the following conclusions:

(1) On a broad scale the spatiotemporal occurrence of early-stage seismicity is in agreeance with modeled pore pressure diffusion. Our model indicates that pore pressure first became elevated on the N. Trinidad fault zone followed by the Vermejo Park fault zone and lastly the Tercio fault zone. This pattern is similar to the migration of seismicity observed in the Raton Basin after injection started.

(2) The initial seismicity of the August – September 2001 earthquakes sequence was likely triggered by pore pressure perturbation between 0.007 – 0.03 MPa. Three of the fifteen active injection wells, Cottontail Pass, PCW and Wild Boar, produced 92% of the pore pressure change. The Cottontail Pass well produced the majority of the

perturbation making it the most influential well in triggering the August – September 2001 earthquakes sequence, even though it was the furthest of the three wells from the fault zone. Closer wells produced less perturbation in the fault zone because they had been injecting for substantially less time and the basal sedimentary interval restricted vertical pore pressure diffusion, thus delaying pore pressure perturbation generated by these wells.

(3) Given the available data, a precise date of early-stage seismicity could not be deduced for the Vermejo Park and Tercio fault zone, but it is very likely that the Vermejo Park fault zone was reactivated prior to the Tercio fault zone. At the average seismicity depths, the fault zones reached the estimated triggering threshold at a time that is likely too late to match the actual timing of early-stage seismicity. This could indicate early-stage seismicity was shallower than expected or there are hydrogeologic heterogeneities that allowed for enhanced pore pressure diffusion.

(4) Model sensitivity to varying the diffusivity of the injection interval and fault zones suggest that diffusivity of the injection interval affects modeled pore pressure perturbation at all depths along the fault zone. The fault zone diffusivity plays a muted role at shallows depths but highly affects pore pressure perturbation at greater depths.

(5) For most hydrogeologic scenarios the homogeneous low diffusivity basement produced substantially greater pore pressure perturbation within the fault zones than the depth decaying diffusivity basement. The homogeneous low diffusivity basement prohibited vertical pore pressure propagation into the unfaulted sections of the basement, concentrating pore pressure diffusion into the top of the fault zones. The depth decaying basement allowed pore pressure to propagate deeper into the unfaulted

sections of the basement which allowed pore pressure diffusion into both the top and sides of the fault zones. When modeling a sealing fault zone pore pressure increase at moderate and deep depths was similar when comparing the two basement representations. This highlights that pore pressure perturbation in a fault zone is more dependent on fault zone diffusivity when modeling a homogenous low diffusivity basement. The hydrogeologic properties of the basement substantially affects pore pressure diffusion and should be considered in future hydro-mechanical models.

# References

Baldwin, B., & Muehlberger, W. R. (1959). *Geologic studies of Union County, New Mexico*. State Bureau of Mines and Mineral Resources, New Mexico Institute of Mining & Technology, Campus Station.

Baltz, E. H. (1965). Stratigraphy and history of the Raton basin and notes on San Luis basin, Colorado-New Mexico. *American Association of Petroleum Geologists Bulletin*, 49, 2041–2075. https://doi.org/10.1306/a6633882-16c0-11d7-8645000102c1865d

Barnhart, W. D., Benz, H. M., Hayes, G. P., Rubinstein, J. L., & Bergman, E. (2014). Seismological and geodetic constraints on the 2011 Mw5. 3 Trinidad, Colorado earthquake and induced deformation in the Raton Basin. *Journal of Geophysical Research: Solid Earth*, *119*(10), 7923-7933. https://doi.org/10.1002/2014JB011227

Blondes, M.S., Gans, K.D., Engle, M.A., Kharaka, Y.K., Reidy, M.E., Saraswathula, V., et al. (2018). *U.S. Geological Survey National Produced Waters Geochemical Database* (ver. 2.3, January 2018): U.S. Geological Survey data release, https://doi.org/10.5066/F7J964W8.

Bohlen, K. (2013). Pre-Exploration Geothermal Resource Assessment for the Raton Basin, Colorado - The rest of the story: *GRC Transactions*, 37, 933-940.

Bredehoeft, J. D., Neuzil, C. E., & Milly, P. C. D. (1983). Regional flow in the Dakota aquifer: A study of the role of confining layers (Vol. 2237). USGS Water Supply Paper 223.

Brown, C. E. (1998). Applied multivariate statistics in geohydrology and related sciences. Berlin; New York: Springer. Retrieved from http://catalog.hathitrust.org/api/volumes/oclc/37341457.html

Brown, M. R., Ge, S., Sheehan, A. F., & Nakai, J. S. (2017). Evaluating the effectiveness of induced seismicity mitigation: Numerical modeling of wastewater injection near Greeley, Colorado. *Journal of Geophysical Research: Solid Earth*, *122*(8), 6569-6582. https://doi.org/10.1002/2017JB014456

Bucher, K., & Stober, I. (2010). Fluids in the upper continental crust. *Geofluids*, *10*(1-2), 241-253. https://doi.org/10.1111/j.1468-8123.2010.00279.x

Caine, J. S., Evans, J. P., & Forster, C. B. (1996). Fault zone architecture and permeability structure. *Geology*, *24*(11), 1025-1028. https://doi.org/10.1130/0091-7613(1996)024<1025:FZAAPS>2.3.CO;2

Chang, K. W., & Segall, P. (2016). Injection-induced seismicity on basement faults including poroelastic stressing. *Journal of Geophysical Research: Solid Earth*, *121*(4), 2708-2726. https://doi.org/10.1002/2015JB012561

Clark, K. F., & Read, C. B. (1972). *Geology and ore deposits of Eagle Nest area, New Mexico*. New Mexico State Bureau of Mines and Mineral Resources.

Colorado Oil and Gas Conservation Commission (2020). Colorado Oil and Gas Conservation Commission, COGCC website. [Retrieved from http://cogcc.state.co.us/data.html#/cogis.] (Accessed 20 July 2020)

EORC, J. (2016). ALOS global digital surface model "ALOS World 3D-30m"(AW3D30).

Fan, Z., Eichhubl, P., & Newell, P. (2019). Basement fault reactivation by fluid injection into sedimentary reservoirs: Poroelastic effects. *Journal of Geophysical Research: Solid Earth*, 124, 7354–7369. https://doi.org/10.1029/2018JB017062

Fetter, C. W. (2018). Applied hydrogeology. Waveland Press.

Fridrich, C. J., Shroba, R. R., & Hudson, A. M. (2012). *Preliminary Geologic Map of the Big Costilla Peak Area, Taos County, New Mexico, and Costilla County, Colorado*. U. S. Geological Survey. Open-File Report OF-2012-1041.

Garavito, A. M., Kooi, H., & Neuzil, C. E. (2006). Numerical modeling of a long-term in situ chemical osmosis experiment in the Pierre Shale, South Dakota. *Advances in Water Resources*, *29*(3), 481–492. https://doi.org/10.1016/j.advwatres.2005.06.004

Garrabrant, L. A. (1993). *Water Resources of Taos County, New Mexico* (Vol. 93, No. 4107). U. S. Geological Survey. Open-File Report OF-93-4107.

Geldon, A. L. (1989). Ground-water hydrology of the central Raton Basin, Colorado and New Mexico. U. S. Geological Survey Water-Supply Paper, 2288, 1–81.

Glasgow, M., Schmandt, B., Wang, R., Zhang, M., Bilek, S. L., & Kiser, E. (2021). Raton Basin induced seismicity is hosted by networks of short basement faults and mimics tectonic earthquake statistics. Journal of Geophysical Research: Solid Earth, 126, e2021JB022839. https://doi.org/10.1029/2021JB022839

Goebel, T. H., Weingarten, M., Chen, X., Haffener, J., & Brodsky, E. E. (2017). The 2016 Mw5.1 Fairview, Oklahoma earthquakes: Evidence for long-range poroelastic triggering at >40 km from fluid disposal wells. *Earth and Planetary Science Letters*, 472, 50–61. https://doi.org/10.1016/j.epsl.2017.05.011

Gries, J. P., Rahn, P. H., & Baker, R. K. (1976). *A pump test in the Dakota Sandstone at Wall, South Dakota*. Science Center, University of South Dakota.

Harbaugh, A. W., Banta, E. R., Hill, M. C., & Macdonald, M. G. (2000). The US geological survey modular ground water models: User guide to modulization concepts and the groundwater flow process. *US Geological Survey*, *121*.

Healy, J. H., Rubey, W. W., Griggs, D. T., & Raleigh, C. B. (1968). The Denver Earthquakes. *Science*, *161*(3848), 1301–1310. https://doi.org/10.1126/science.161.3848.1301

Hemborg, H. T. (1996). *Basement structure map of Colorado with major oil and gas fields*. Colorado Geological Survey, Department of Natural Resources.

Hernandez, R., & Weingarten, M. (2019, December). Step-rate Test Calibration of Primary Injection Reservoir Permeability in a Case of Injection Induced Seismicity, Raton Basin, CO-NM. In *AGU Fall Meeting Abstracts* (Vol. 2019, pp. S13E-0493).

Herrmann, R. B. (2020). North America moment tensor 1995–2020, St. Louis Univ. website. [Retrieved from http://www.eas.slu.edu/eqc/eqc_mt/MECH.NA/.] (Accessed 10 December 2020)

Hornbach, M. J., DeShon, H. R., Ellsworth, W. L., Stump, B. W., Hayward, C., Frohlich, C., et al. (2015). Causal factors for seismicity near Azle, Texas. Nature Communications, 6(6728), 1–11. https://doi.org/10.1038/ncomms7728

Hubbert, M. K., & Rubey, W. W. (1959). Role of fluid pressure in mechanics of overthrust faulting: I. Mechanics of fluid-filled porous solids and its application to overthrust faulting. *Geological Society of America Bulletin*, *70*(2), 115-166. https://doi.org/10.1130/0016-7606(1961)72[1445:ROFPIM]2.0.CO;2

Huber, M. L., Perkins, R. A., Laesecke, A., Friend, D. G., Sengers, J. V., Assael, M. J., et al. (2009). New International Formulation for the Viscosity of H2O. *Journal of Physical and Chemical Reference Data*, *38*(2), 101–125. https://doi.org/10.1063/1.3088050

Johnson, R. B. (1969). *Geologic map of the Trinidad quadrangle, south-central Colorado*. U. S. Geological Survey. Open-File Report OF-558.

Johnson, R. B. (1975). *Geologic map of the Rainsville quadrangle, Mora County, New Mexico*. U. S. Geological Survey. Open-File Report OF-1276

Johnson, R. B. (1974). *Geologic map of the Fort Union quadrangle, Mora County, New Mexico*. U. S. Geological Survey. Open-File Report OF-1164.

Kelley, S. A. (2015). Geothermal potential of the Raton Basin, New Mexico, New Mexico Geological Society. Guidebook 66 - Geology of the Las Vegas Area, New Mexico Geological Society 66th Annual Fall Field Conference Guidebook, 261 – 275.

Keranen, K. M., Weingarten, M., Abers, G. A., Bekins, B. A., & Ge, S. (2014). Sharp increase in central Oklahoma seismicity since 2008 induced by massive wastewater injection. *Science*, *345*(6195), 448–451. https://doi.org/10.1126/science.1255802

King, G. C., Stein, R. S., & Lin, J. (1994). Static stress changes and the triggering of earthquakes. *Bulletin of the Seismological Society of America*, *84*(3), 935-953. https://doi.org/10.1016/0148-9062(95)94484-2

Kuang, X., & Jiao, J. J. (2014). An integrated permeability-depth model for Earth's crust. *Geophysical Research Letters*, *41*(21), 7539-7545. https://doi.org/10.1002/2014GL061999

Lindsey, D. A. (1995a). *Geologic map of the McCarty Park Quadrangle, Costilla and Huerfano counties, Colorado*. U. S. Geological Survey. Open-File Report OF-2282.

Lindsey, D. A. (1995b). *Geologic map of the Cuchara Quadrangle, Huerfano County, Colorado*. U. S. Geological Survey. Open-File Report OF-2283.

Lindsey, D. A. (1996). *Reconnaissance geologic map of the Cucharas Pass quadrangle, Huerfano and Las Animas Counties, Colorado*. U. S. Geological Survey. Open-File Report OF-2294.

Manning, C. E., & Ingebritsen, S. E. (1999). Permeability of the continental crust: Implications of geothermal data and metamorphic systems. *Reviews of Geophysics*, *37*(1), 127-150. https://doi.org/10.1029/1998RG900002

Meremonte, M. E., Lahr, J. C., Frankel, A. D., Dewey, J. W., Crone, A. J., Overturf, D., et al. (2002). *Investigation of an earthquake swarm near Trinidad, Colorado, August-October 2001* (No. 2002-73). US Geological Survey. Open-File Rept. 02-0073.

Morgan, P. (2009). A preliminary analysis of geothermal resources in the central Raton Basin, Colorado, from bottom-hole temperature data. *Geothermal Resources Council, Transactions*, *33*, 509-513.

Nakai, J. S., Sheehan, A. F., & Bilek, S. L. (2017a). Seismicity of the rocky mountains and Rio Grande Rift from the EarthScope Transportable Array and CREST temporary seismic networks, 2008–2010. *Journal of Geophysical Research: Solid Earth*, *122*(3), 2173-2192. https://doi.org/10.1002/2016JB013389

Nakai, J. S., Weingarten, M., Sheehan, A. F., Bilek, S. L., & Ge, S. (2017b). A possible causative mechanism of Raton Basin, New Mexico and Colorado earthquakes using recent seismicity patterns and pore pressure modeling. *Journal of Geophysical Research: Solid Earth*, *122*(10), 8051-8065. https://doi.org/10.1002/2017jb014415

Nelson, P. H., Gianoutsos, N. J., & Anna L. O. (2013), Outcrop control of basin-scale underpressure in the Raton Basin, Colorado and New Mexico, Mt. Geol. 50, no. 2, 37–63.

New Mexico Oil Conservation Division. (2020). New Mexico Oil and Conservation Division, 2016, permitting. [Retrieved from https://wwwapps.emnrd.state.nm.us/ocd/ocdpermitting/data/wells.aspx] (Accessed 20 July 2020)

Norbeck, J. H., & Horne, R. N. (2018). Maximum magnitude of injection-induced earthquakes: A criterion to assess the influence of pressure migration along faults. *Tectonophysics*, *733*, 108-118. https://doi.org/10.1016/j.tecto.2018.01.028

Ogwari, P. O., DeShon, H. R., & Hornbach, M. J. (2018). The Dallas-Fort Worth airport earthquake sequence: Seismicity beyond injection period. *Journal of Geophysical Research: Solid Earth*, *123*(1), 553-563. https://doi.org/10.1002/2017JB015003

Pillmore, C. L. (2003). Geologic map of the Vermejo Park quadrangle, Colfax County, New Mexico, and Las Animas County, Colorado. U. S. Geological Survey. Open-File Report OF-2003-438.

Pollyea, R. M., Chapman, M. C., Jayne, R. S., & Wu, H. (2019). High density oilfield wastewater disposal causes deeper, stronger, and more persistent earthquakes. *Nature communications*, *10*(1), 1-10. https://doi.org/10.1038/s41467-019-11029-8

Pollyea, R. M., Konzen, G. L., Chambers, C. R., Pritchard, J. A., Wu, H., & Jayne, R. S. (2020). A new perspective on the hydraulics of oilfield wastewater disposal: how PTX conditions affect fluid pressure transients that cause earthquakes. *Energy & Environmental Science*, *13*(9), 3014-3031. https://doi.org/10.1039/D0EE01864C

Reasenberg, P. A., & Simpson, R. W. (1992). Response of regional seismicity to the static stress change produced by the Loma Prieta earthquake. *Science*, *255*(5052), 1687-1690. https://doi.org/10.1126/science.255.5052.1687

Ree, J. H., Kim, J. H., Park, C., Kim, C. M., Han, R., Shimamoto, T., & Kang, H. C. (2018, December). Proxies for the 2017 Pohang Earthquake Fault and Modelling of Fluid Flow. In *AGU Fall Meeting Abstracts* (Vol. 2018, pp. S23B-0519).

Robinson, G. D. V., Wanek, A. A., Hays, W. H., & McCallum, M. E. (1964). *Philmont Country: the rocks and landscape of a famous New Mexico ranch*. US Government Printing Office.

Rubinstein, J. L., Ellsworth, W. L., McGarr, A., & Benz, H. M. (2014). The 2001-Present Induced Earthquake Sequence in the Raton Basin of Northern New Mexico and

Southern Colorado. *Bulletin of the Seismological Society of America*, *104*(5), 2162–2181. https://doi.org/10.1785/0120140009

Saar, M. O., & Manga, M. (2004). Depth dependence of permeability in the Oregon Cascades inferred from hydrogeologic, thermal, seismic, and magmatic modeling constraints. *Journal of Geophysical Research: Solid Earth*, *109*(B4). https://doi.org/10.1029/2003JB002855

Savage, H. M., & Brodsky, E. E. (2011). Collateral damage: Evolution with displacement of fracture distribution and secondary fault strands in fault damage zones. *Journal of Geophysical Research: Solid Earth*, *116*(B3), B03405. https://doi.org/10.1029/2010JB007665

Stein, R. S. (1999). The role of stress transfer in earthquake occurrence. Nature, 402(6762), 605-609. https://doi.org/10.1038/45144

Stober, I., & Bucher, K. (2007). Hydraulic properties of the crystalline basement. *Hydrogeology Journal*, *15*(2), 213-224. https://doi.org/10.1007/s10040-006-0094-4

Stober, I. (2011). Depth-and pressure-dependent permeability in the upper continental crust: data from the Urach 3 geothermal borehole, southwest Germany. *Hydrogeology Journal*, *19*(3), 685-699. https://doi.org/10.1007/s10040-011-0704-7

Teeple, A. P., Ging, P. B., Thomas, J. V., Wallace, D. S., & Payne, J. D. (2021). *Hydrogeologic framework, geochemistry, groundwater-flow system, and aquifer hydraulic properties used in the development of a conceptual model of the Ogallala, Edwards-Trinity (High Plains), and Dockum aquifers in and near Gaines, Terry, and Yoakum Counties, Texas* (No. 2021-5009). US Geological Survey.

Tung, S., Zhai, G., & Shirzaei, M. (2021). Potential link between 2020 Mentone, West Texas M5 earthquake and nearby wastewater injection: Implications for aquifer mechanical properties. Geophysical Research Letters, 48, e2020GL090551.https://doi.org/10.1029/2020GL09055

Vine, J. D. (1974). *Geologic Map and Cross Sections of the La Veta Pass, La Veta, and Ritter Arroyo Quadrangles, Huerfano and Costilla Counties, Colorado* (No. 833).

Wagner, W., & Pruß, A. (2002). The IAPWS formulation 1995 for the thermodynamic properties of ordinary water substance for general and scientific use. *Journal of physical and chemical reference data*, *31*(2), 387-535. https://doi.org/10.1063/1.1461829

Wallace, A. R., & Lindsey, D. A. (1996). *Geologic map of the Trinchera Peak Quadrangle, Costilla, Huerfano, and Las Animas counties, Colorado*. U. S. Geological Survey. Open-File Report OF-2312.

Wanek, A. A., Read, C. B., Robinson, G. D., Hays, W. H., & McCallum, M. (1959). *Geologic map and geologic sections of Philmont Ranch quadrangle, New Mexico* (No. 59-126). U. S. Geological Survey. Open-File Report OF-425.

Weingarten, M., Ge, S., Godt, J. W., Bekins, B. A., & Rubinstein, J. L. (2015). High-rate injection is associated with the increase in US mid-continent seismicity. *Science*, *348*(6241), 1336-1340. https://doi.org/10.1126/science.aab1345

Xue, L., Li, H. B., Brodsky, E. E., Xu, Z. Q., Kano, Y., Wang, H., et al. (2013). Continuous permeability measurements record healing inside the Wenchuan earthquake fault zone. *Science*, *340*(6140), 1555-1559. https://doi.org/10.1126/science.1237237

Yeo, I. W., Brown, M. R. M., Ge, S., & Lee, K. K. (2020). Causal mechanism of injection-induced earthquakes through the M w 5.5 Pohang earthquake case study. *Nature communications*, *11*(1), 1-12. https://doi.org/10.1038/s41467-020-16408-0

Zhai, G., Shirzaei, M., Manga, M., & Chen, X. (2019). Pore-pressure diffusion, enhanced by poroelastic stresses, controls induced seismicity in Oklahoma. *Proceedings of the National Academy of Sciences*, *116*(33), 16228-16233. https://doi.org/10.1073/pnas.1819225116

Zhang, Y., Person, M., Rupp, J., Ellett, K., Celia, M. A., Gable, C. W., et al. (2013). Hydrogeologic controls on induced seismicity in crystalline basement rocks due to fluid injection into basal reservoirs. *Groundwater*, *51*(4), 525-538. https://doi.org/10.1111/gwat.12071

# Appendix A. Data and Model Details

## A.1 Injection Data

Reported water production from the New Mexico Oil Conservation Division (NMOCD, 2020) was used to estimate the injection for the six New Mexico wells that were injecting prior to June 2006. To assign injection rates from production data, the percent contribution was calculated for each well between June 2006 to May 2008. During this time interval, all six wells were injecting, and the actual injection totals were being reported. By comparing the individual wells injection totals to the cumulative injection totals, from June 2006 to May 2008, a percent contribution for each well was calculated. Given the six wells started injecting at different times between October 1999 to September 2005, the wells percent contribution was normalized based on which wells were injecting. The percent contributions and the reported produced water was then used to determine approximate monthly injection totals for the six wells from October 1999 through May 2006.

**Table A-1. Injection Well Details**

| Age number | Well name | Well API | Starting date (Mo,Yr) | State | Screened interval elevations (m) |
|---|---|---|---|---|---|
| 1 | COTTONTAIL PASS DISPOSAL WELL #32-33 | 071-06106 | Nov-94 | CO | 378-291 |
| 2 | APACHE CANYON #10-3 | 071-06126 | Jan-95 | CO | 479-462 |
| 3 | APACHE CANYON #19-10 | 071-06123 | Jan-95 | CO | 366-307 |
| 4 | PCW #12-4 | 071-06421 | Jul-97 | CO | 710-661 |
| 5 | VPR C #14 | 071-06867 | Sep-99 | CO | 626-454, 381-359 |
| 6 | VPR A #007 | 007-20116 | Oct-99 | NM | 511-461 |
| 7 | SAWTOOTH #34-4 | 071-06706 | Apr-00 | CO | 729-690 |
| 8 | VPR C #39 | 071-06946 | May-00 | NM | 483-458, 386-377 |
| 9 | VPR A #042 | 007-20143 | May-00 | CO | 465-254 |
| 10 | VPR B #027 | 007-20161 | Jul-00 | NM | 339-196 |
| 11 | WILD BOAR #21-32 | 071-06741 | Aug-00 | CO | 731-696 |
| 12 | VPR D #025 | 007-20152 | Sep-00 | NM | 633-606, 441-414 |
| 13 | BEARDON #24-15 | 071-07016 | Jan-01 | CO | 790-762 |
| 14 | LONG CANYON #43-12 | 071-07035 | Apr-01 | CO | 817-803, 786-762 |
| 15 | LA GARITA #42-20 | 071-07045 | Aug-01 | CO | 552-534 |
| 16 | VPR E #099 | 007-20378 | Jan-03 | NM | 544-280 |
| 17 | WESTON #24-23 A | 071-07690 | Jan-04 | CO | 468-438 |
| 18 | CIMARRON #32-18 | 071-07565 | Mar-05 | CO | 310-277 |
| 19 | DEL AGUA #44-2 | 071-07706 | Jul-05 | CO | 563-559 |
| 20 | HILL RANCH DEEP #14-12 | 071-07455 | Jul-05 | CO | 683-651 |
| 21 | VPR A #182 | 007-20540 | Sep-05 | NM | 602-444, 419-324 |
| 22 | JAROSA #32-33 | 071-08532 | May-07 | CO | 494-451 |
| 23 | FERMINIA #12-6 | 071-08889 | Sep-07 | CO | 406-341 |
| 24 | VPR A #500 | 007-20892 | Jun-08 | NM | 763-427 |
| 25 | SOUTHPAW #33-36 | 071-09594 | Apr-09 | CO | 587-530,447-412 |
| 26 | POLLY #23-29 | 071-09728 | Jul-09 | CO | 692-614, 547-509 |
| 27 | LOPEZ CANYON | 071-09733 | Sep-10 | CO | 471-398 ,296-239 |
| 28 | VPR C #204 | 071-09838 | Mar-12 | CO | 598-317 |
| 29 | San Pablo #11-4 | 071-09916 | Dec-14 | CO | 413-317, 237-215 |

## A.2 Structure Maps

Pore pressure diffusion is largely affected by both the hydrogeologic properties and geometric characteristics of the Basin's hydraulically significant units. In most studies the hydrogeologic properties are well documented, but there is often a lack of consideration for the geometry of the basin's geology. When considering structural basins are characterized by spatially variable amounts of tectonic and burial subsidence, that results in significant elevation variations, it is important to consider the geometry of the geologic units. To more accurately model pore pressure diffusion, our numerical model takes into consideration local topography (EORC, 2016) and the elevation variations of the bottom of the hydraulic barrier and top of the Precambrian basement (Figure A1). To construct the structure maps were extracted the elevation of the formation top from well logs and used geologic maps to show where the formation cropped out (Baldwin and Muehlberger, 1959; Clark and Read, 1972; Fridrich et al., 2012; Garrabrant,1993; Johnson, 1969; Johnson, 1974; Johnson , 1975; Lindsey, 1995a; Lindsey, 1995b; Lindsey, 1996; Pillmore, 2003; Vine, 1974; Wallace, 1996; Wanek, 1959). The well logs used for the top of the Dakota Formation (correlates to the bottom of the Hydraulic Barrier) are in Table A-1. The well logs used for the top of the Precambrian basement are in Table A-2, additional data from a published basement structure maps were also used to help fill in gaps where well logs did not exist (Hembog, 1996).
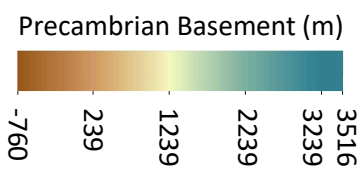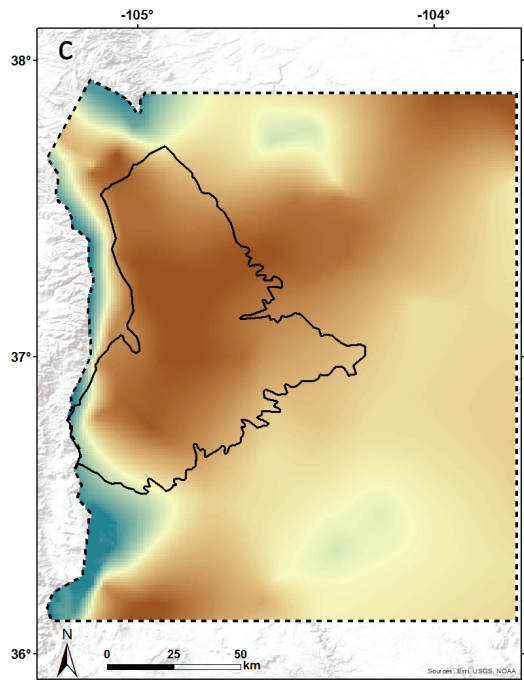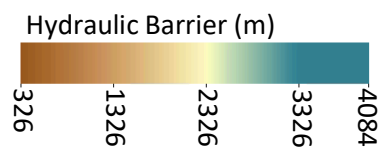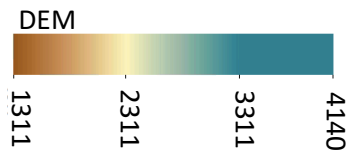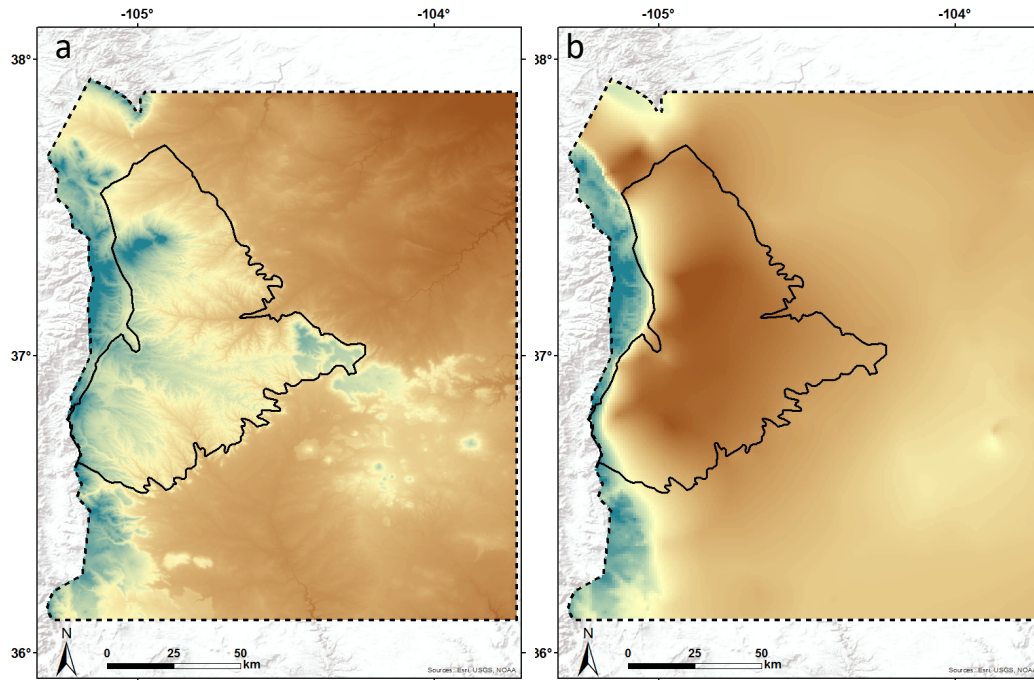
**Figure A-1.** Dem and structure maps developed an implemented into numerical model, solid black line denotes Raton Basin boundary and dashed black line denotes the extent of the model domain. (a) ALOS Global Digital Surface Model with 30m resolution (EORC, 2016). b) Structure map of the bottom of the shale-rich hydraulic barrier. (c) Structure map of the top of the Precambrian basement.

**Table A-2. Wells with Dakota Formation Top Elevations**

| Well Name | Latitude | Longitude | Surface Elevation (masl) | Dakota Depth (masl) | Dakota Top Elevation (masl) |
|---|---|---|---|---|---|
| Freeman #3-24_NonSWD | 37.685 | -105.068 | 2158 | 1793 | 365 |
| 30-007-05007 | 36.347 | -104.328 | 1880 | 55 | 1825 |
| 30-007-05012 | 36.519 | -104.760 | 1908 | 677 | 1231 |
| 30-007-05015 | 36.671 | -104.559 | 1877 | 543 | 1334 |
| 30-007-07001 | 36.274 | -104.831 | 1925 | 251 | 1674 |
| 30-007-07016 | 36.761 | -104.384 | 1905 | 445 | 1460 |
| 30-007-07036 | 36.767 | -104.383 | 1907 | 415 | 1492 |
| 30-007-07044 | 36.224 | -104.657 | 1830 | 277 | 1553 |
| 30-007-20001 | 36.840 | -104.920 | 2213 | 1569 | 644 |
| 30-007-20006 | 36.808 | -104.862 | 2213 | 1507 | 706 |
| 30-007-20008 | 36.810 | -105.009 | 2482 | 1818 | 664 |
| 30-007-20012 | 36.887 | -104.275 | 2523 | 1018 | 1505 |
| 30-007-20014 | 36.383 | -104.708 | 1821 | 308 | 1513 |
| 30-007-20016 | 36.565 | -104.645 | 1857 | 531 | 1326 |
| 30-007-20018 | 36.285 | -104.096 | 1859 | 77 | 1782 |
| 30-007-20019 | 36.402 | -104.243 | 1990 | 151 | 1839 |
| 30-007-20033 | 36.687 | -104.707 | 2031 | 951 | 1080 |
| 30-007-20038 | 36.261 | -104.521 | 1789 | 49 | 1740 |
| 30-007-20039 | 36.720 | -104.532 | 1902 | 609 | 1293 |
| 30-007-20045 | 36.278 | -104.670 | 1850 | 180 | 1670 |
| 30-007-20046 | 36.285 | -104.733 | 1938 | 258 | 1680 |
| 30-007-20047 | 36.619 | -104.748 | 1922 | 829 | 1093 |
| 30-007-20049 | 36.767 | -104.180 | 2083 | 220 | 1863 |
| 30-007-20053 | 36.420 | -104.387 | 1866 | 135 | 1731 |
| 30-007-20054 | 36.532 | -104.351 | 1943 | 161 | 1782 |
| 30-007-20055 | 36.779 | -104.225 | 2032 | 296 | 1736 |
| 30-007-20056 | 36.641 | -104.758 | 1926 | 876 | 1050 |
| 30-007-20057 | 36.521 | -104.445 | 1876 | 252 | 1624 |
| 30-007-20062 | 36.474 | -104.600 | 1793 | 296 | 1497 |
| 30-007-20067 | 36.743 | -104.652 | 2198 | 998 | 1200 |
| 30-007-20071 | 36.749 | -104.731 | 2206 | 1254 | 952 |
| 30-007-20072 | 36.742 | -104.647 | 2084 | 980 | 1104 |
| 30-007-20075 | 36.745 | -104.633 | 2120 | 900 | 1220 |
| 30-007-20077 | 36.751 | -104.399 | 1910 | 400 | 1510 |

| | | | | | |
|---|---|---|---|---|---|
| 30-007-20116 | 36.955 | -104.871 | 2529 | 1951 | 578 |
| 30-007-20378 | 36.954 | -104.939 | 2621 | 1985 | 636 |
| 30-007-90009 | 36.958 | -104.776 | 2414 | 1787 | 627 |
| 30-007-90012 | 36.895 | -104.668 | 2374 | 1469 | 905 |
| 30-007-90015 | 36.890 | -104.560 | 2085 | 945 | 1140 |
| 30-007-90019 | 36.803 | -105.133 | 2601 | 1577 | 1024 |
| 30-007-90027 | 36.832 | -104.548 | 2324 | 995 | 1329 |
| 30-007-90028 | 36.840 | -104.643 | 2369 | 1364 | 1005 |
| 30-007-90029 | 36.819 | -104.639 | 2357 | 1375 | 982 |
| 30-007-90036 | 36.752 | -104.610 | 1980 | 745 | 1235 |
| 30-007-90037 | 36.747 | -104.624 | 1994 | 841 | 1153 |
| 30-007-90040 | 36.673 | -104.777 | 1950 | 975 | 975 |
| 30-007-90041 | 36.679 | -104.668 | 1978 | 876 | 1102 |
| 30-007-90044 | 36.674 | -104.167 | 2128 | 104 | 2024 |
| 30-007-90046 | 36.563 | -104.641 | 1856 | 546 | 1310 |
| 30-007-90049 | 36.522 | -104.365 | 1911 | 132 | 1779 |
| 30-007-90050 | 36.362 | -104.975 | 2101 | 177 | 1924 |
| 30-007-90051 | 36.401 | -104.861 | 1924 | 424 | 1500 |
| 30-007-90053 | 36.219 | -104.383 | 1795 | 11 | 1784 |
| 30-033-20001 | 36.162 | -104.939 | 2128 | 229 | 1899 |
| 30-033-20002 | 36.180 | -104.575 | 1899 | 245 | 1654 |
| 30-033-20006 | 36.031 | -104.666 | 1891 | 126 | 1765 |
| 30-033-20008 | 36.041 | -104.672 | 1889 | 93 | 1796 |
| 30-033-20010 | 36.027 | -104.675 | 1882 | 114 | 1768 |
| 30-033-20015 | 36.104 | -104.755 | 2009 | 395 | 1614 |
| 30-033-20016 | 36.155 | -104.644 | 1863 | 298 | 1565 |
| 30-033-20017 | 36.126 | -104.653 | 1890 | 288 | 1602 |
| 30-033-20030 | 36.060 | -104.402 | 1840 | 1 | 1840 |
| 30-033-20037 | 36.060 | -104.679 | 1892 | 124 | 1768 |
| 30-033-20040 | 36.053 | -104.679 | 1888 | 112 | 1776 |
| 30-033-20043 | 35.890 | -104.960 | 2035 | 1 | 2035 |
| 30-033-20044 | 35.941 | -104.475 | 1880 | 1 | 1880 |
| 30-033-20046 | 36.075 | -104.734 | 1946 | 306 | 1640 |
| 30-033-20047 | 35.938 | -104.591 | 1836 | 73 | 1763 |
| 30-033-20050 | 36.038 | -104.715 | 1949 | 184 | 1765 |
| 30-033-20061 | 36.191 | -104.629 | 1851 | 281 | 1570 |
| ANNIE BELL | 36.723 | -104.542 | 1911 | 609 | 1302 |
| APACHE_CANYON #19-10 | 37.069 | -104.926 | 2245 | 1686 | 559 |
| APACHE_CANYON_10-3 | 37.103 | -104.986 | 2640 | 1930 | 710 |
| ARCO CF & I #1 | 36.997 | -104.971 | 2650 | 1373 | 1277 |

| | | | | | |
|---|---|---|---|---|---|
| BEARDON #24-15 WD | 37.253 | -104.663 | 2290 | 1498 | 792 |
| BRANSON #1 | 37.029 | -103.884 | 1889 | 9 | 1880 |
| Caddell #2 | 37.552 | -105.112 | 2391 | 1573 | 818 |
| Caddell #3 | 37.552 | -105.112 | 2391 | 1689 | 702 |
| CANADIAN RIVER #1 | 36.998 | -105.050 | 2770 | 1921 | 849 |
| CHALFONT-KAISER | 36.745 | -104.644 | 2099 | 989 | 1110 |
| CIMARRON #32-18 WD | 37.259 | -104.926 | 2426 | 2113 | 313 |
| COPPA #1 | 37.464 | -104.627 | 1929 | 368 | 1561 |
| COTTONTAIL PASS DISPOSAL WELL #32-33 | 37.216 | -104.780 | 2277 | 1746 | 531 |
| CRAIGHEAD #1 | 37.861 | -103.636 | 1340 | 168 | 1172 |
| CROKE ET AL (OWP) #1-21 | 37.677 | -104.777 | 1835 | 682 | 1153 |
| CUERNO VERDE RANCH #1 | 37.855 | -105.330 | 2369 | 851 | 1518 |
| D A GAULKE #1 | 37.788 | -103.658 | 1390 | 107 | 1283 |
| DEL AGUA #44-2 WD | 37.281 | -104.745 | 2297 | 1731 | 566 |
| DIKE MOUNTAIN UNIT #4-13 | 37.614 | -105.175 | 3032 | 1587 | 1445 |
| DIKE MOUNTAIN UNIT #7-7 | 37.622 | -105.149 | 2662 | 2013 | 649 |
| DORTHEA MAE #1 | 38.157 | -104.439 | 1451 | 332 | 1119 |
| E K WARREN AND SON #1 | 38.043 | -104.943 | 1996 | 43 | 1953 |
| El_Paso_VPR_A_007 | 36.961 | -104.829 | 2462 | 1872 | 590 |
| El_Paso_VPR_A_042 | 36.953 | -104.873 | 2528 | 1943 | 585 |
| El_Paso_VPR_A_182 | 36.981 | -104.824 | 2471 | 1868 | 603 |
| El_Paso_VPR_A_500 | 36.886 | -104.746 | 2427 | 1661 | 766 |
| El_Paso_VPR_B_027 | 36.796 | -104.974 | 2438 | 1931 | 507 |
| El_Paso_VPR_E_099 | 36.954 | -104.939 | 2624 | 1985 | 639 |
| ElPaso_VPR_D_025 | 36.859 | -105.057 | 2590 | 1957 | 633 |
| FEDERAL #12-23 | 37.770 | -103.767 | 1460 | 131 | 1329 |
| FERMINIA #12-6 WD | 37.291 | -104.829 | 2240 | 1834 | 406 |
| GARCIA (EPA) #1-WD | 37.656 | -105.181 | 2614 | 1226 | 1388 |
| GOVERNMENT #1-34 | 37.655 | -104.768 | 1861 | 722 | 1139 |
| GOVT. CYNTHIA TRUE #1 | 37.582 | -103.730 | 1630 | 1 | 1630 |
| GRIFFITH #1 | 37.819 | -105.284 | 2292 | 1730 | 562 |
| GRIFFITH #1-12 | 37.801 | -105.279 | 2278 | 1135 | 1143 |
| Harriman #1 | 37.984 | -104.002 | 1388 | 300 | 1088 |

| | | | | | |
|---|---|---|---|---|---|
| HILL RANCH DEEP #14-12 WD | 37.093 | -104.736 | 2146 | 1460 | 686 |
| HOFF HEIRS #2 | 37.479 | -104.086 | 1688 | 18 | 1670 |
| HOMERDING #1 | 37.713 | -104.947 | 1949 | 666 | 1283 |
| JACKSON, ROBERT A. #1 | 38.194 | -104.704 | 1621 | 141 | 1480 |
| JAROSA #32-33 WD | 37.305 | -104.783 | 2161 | 1664 | 497 |
| JOHNSTON 'A' #1 | 37.932 | -104.186 | 1439 | 146 | 1293 |
| JOLLY #12-17 | 37.437 | -104.590 | 1898 | 365 | 1533 |
| JORDAN GOV #1-X | 37.908 | -103.860 | 1354 | 1 | 1354 |
| JORDAN-GOV #1 | 37.883 | -103.979 | 1436 | 1 | 1436 |
| LA GARITA #42-20 WD | 37.160 | -104.797 | 2180 | 1624 | 556 |
| LANDON K MOORE #001 | 36.767 | -104.383 | 1908 | 416 | 1492 |
| LITTLE #1 | 37.946 | -104.675 | 1752 | 176 | 1576 |
| LONG CANYON #43-12 WD | 37.096 | -104.616 | 1945 | 1125 | 820 |
| LOPEZ CANYON SWD #1 | 37.155 | -104.890 | 2224 | 1751 | 473 |
| LOUDEN #1 | 37.044 | -103.707 | 1786 | 11 | 1775 |
| LUTIN #1 | 38.187 | -104.706 | 1616 | 121 | 1495 |
| MAJORS #42-4 | 37.644 | -104.998 | 2122 | 1077 | 1045 |
| MCCOMBS #5 | 37.643 | -104.847 | 1975 | 1162 | 813 |
| MIRAH #1 | 37.109 | -104.339 | 1894 | 594 | 1300 |
| MOORE | 36.761 | -104.385 | 1905 | 410 | 1495 |
| MOORE #002 | 36.761 | -104.385 | 1905 | 410 | 1495 |
| MOORE RANCH - STATE #001 | 36.753 | -103.859 | 2057 | 400 | 1657 |
| Moore_2 | 36.767 | -104.383 | 1908 | 410 | 1498 |
| no API listed | 36.216 | -104.657 | 1811 | 302 | 1509 |
| ODESSA NATURAL CORP W S RANCH | 36.809 | -104.815 | 2194 | 1494 | 700 |
| ODESSA NATURAL CORP WS RANCH | 36.761 | -104.948 | 2357 | 1884 | 473 |
| ODESSA NATURAL CORP. W S RANCH | 36.829 | -104.975 | 2433 | 1818 | 615 |
| PCW #12-4 WD | 37.116 | -104.683 | 1972 | 1263 | 709 |
| PETERSON-FEDERAL #1-8 | 37.886 | -103.475 | 1378 | 133 | 1245 |
| PHELPS DODGE | 36.674 | -104.734 | 2195 | 974 | 1221 |
| PHELPS DODGE #001Y | 36.752 | -104.693 | 2269 | 1254 | 1015 |
| PHELPS-DODGE | 36.674 | -104.678 | 2096 | 882 | 1214 |
| POLLY #23-29 WD R | 37.227 | -104.698 | 2124 | 1423 | 701 |
| PORTER #1-28 | 38.193 | -104.223 | 1375 | 541 | 834 |

| | | | | | |
|---|---|---|---|---|---|
| PRE-ONGARD WELL | 36.971 | -105.122 | 2696 | 1144 | 1552 |
| PRE-ONGARD WELL | 36.887 | -104.275 | 2521 | 1018 | 1503 |
| PRE-ONGARD WELL #001 | 36.521 | -104.365 | 1910 | 137 | 1773 |
| PRE-ONGARD WELL OPERATOR | 36.887 | -104.275 | 2521 | 1018 | 1503 |
| Robert_19-9 | 37.065 | -104.271 | 1899 | 535 | 1364 |
| Robert_30-10 | 37.051 | -104.272 | 2057 | 701 | 1356 |
| Roberts18-10 | 37.079 | -104.274 | 1787 | 457 | 1330 |
| SALT CREEK RANCH #1 | 37.178 | -104.063 | 1697 | 1 | 1697 |
| SAM TAYLOR #1 | 37.786 | -105.279 | 2318 | 1220 | 1098 |
| San Pablo #11-4 WD | 37.206 | -104.899 | 2294 | 1879 | 415 |
| SANDOVAL #1-1 | 37.109 | -104.296 | 1805 | 447 | 1358 |
| SAWTOOTH #34-4 WD | 37.196 | -104.674 | 2075 | 1344 | 731 |
| SHEEP MOUNTAIN UNIT #3-15-B | 37.703 | -105.210 | 2585 | 1073 | 1512 |
| SOUTHPAW #33-36 WD | 37.299 | -104.729 | 2185 | 1596 | 589 |
| SPORLEDER #1-26 | 37.761 | -104.849 | 1846 | 671 | 1175 |
| STATE #1 | 37.602 | -104.336 | 1719 | 45 | 1674 |
| THATCHER #1 | 38.325 | -104.414 | 1460 | 781 | 679 |
| TRUE STATE #23-16 | 38.046 | -104.016 | 1344 | 303 | 1041 |
| U S A #1 | 37.536 | -104.333 | 1733 | 44 | 1689 |
| VERMEJO PARK | 36.843 | -104.881 | 2264 | 1568 | 696 |
| VERMEJO PARK #002 | 36.843 | -104.881 | 2264 | 1569 | 695 |
| VPR "A" | 36.969 | -104.861 | 2473 | 1881 | 592 |
| VPR "A" #006A | 36.969 | -104.861 | 2473 | 1882 | 591 |
| VPR C #14 WDW | 37.023 | -104.781 | 2380 | 1754 | 626 |
| VPR C #204 WDW | 37.023 | -104.832 | 2246 | 1640 | 606 |
| VPR C #39 | 37.023 | -104.783 | 2384 | 1745 | 639 |
| W.S. SIDNEY #1 | 37.991 | -103.993 | 1401 | 310 | 1091 |
| WESTON #24-23 A WD | 37.151 | -104.860 | 2149 | 1676 | 473 |
| WILD BOAR #21-32 WD | 37.133 | -104.697 | 1988 | 1255 | 733 |
| WILLIAM M WHITE #1 | 38.261 | -104.531 | 1404 | 385 | 1019 |
| Williams 8-11 | 37.094 | -104.260 | 1765 | 427 | 1338 |

**Table A-3. Wells with Precambrian Basement Elevations**

| Well_Name | Latitude | Longitude | Surface Elevation (masl) | Basement Depth (masl) | Basement Elevation (masl) |
|---|---|---|---|---|---|
| CUERNO VERDE RANCH #1 | 37.855 | -105.330 | 2369 | 2041 | 328 |
| GRIFFITH #1 | 37.819 | -105.284 | 2292 | 2780 | -488 |
| GRIFFITH #1-12 | 37.801 | -105.279 | 2278 | 2185 | 93 |
| SAM TAYLOR #1 | 37.786 | -105.279 | 2318 | 2270 | 48 |
| Unknown | 37.733 | -105.276 | 2324 | 1409 | 915 |
| SHEEP MOUNTAIN UNIT #3-15-B | 37.703 | -105.210 | 2585 | 2123 | 462 |
| DIKE MOUNTAIN UNIT #7-7 | 37.622 | -105.149 | 2662 | 3063 | -401 |
| 30-033-20052 | 36.030 | -105.140 | 2297 | 2718 | -421 |
| 30-007-90019 | 36.803 | -105.133 | 2601 | 2627 | -26 |
| 30-033-20053 | 35.990 | -105.130 | 2165 | 3052 | -887 |
| 30-033-20060 | 36.227 | -105.105 | 2351 | 2335 | 16 |
| Freeman #3-24_NonSWD | 37.685 | -105.068 | 2158 | 2843 | -685 |
| ElPaso_VPR_D_025 | 36.859 | -105.057 | 2590 | 3007 | -417 |
| ODESSA NATURAL CORP. W S RANCH | 36.829 | -104.975 | 2433 | 2868 | -435 |
| El_Paso_VPR_B_027 | 36.796 | -104.974 | 2438 | 2981 | -543 |
| ODESSA NATURAL CORP WS RANCH | 36.761 | -104.948 | 2357 | 2934 | -577 |
| E K WARREN AND SON #1 | 38.043 | -104.943 | 1996 | 791 | 1205 |
| 30-033-20001 | 36.162 | -104.939 | 2128 | 2912 | -784 |
| 30-007-90040 | 36.673 | -104.777 | 1950 | 1741 | 209 |
| 30-007-05012 | 36.519 | -104.760 | 1908 | 1139 | 769 |
| LUTIN #1 | 38.187 | -104.706 | 1616 | 1127 | 489 |
| LITTLE #1 | 37.946 | -104.675 | 1752 | 860 | 892 |
| 30-033-20008 | 36.041 | -104.672 | 1889 | 1143 | 746 |
| 30-007-90037 | 36.747 | -104.624 | 1994 | 1427 | 567 |
| 30-033-20002 | 36.180 | -104.575 | 1899 | 1529 | 370 |
| 30-007-05015 | 36.671 | -104.559 | 1877 | 893 | 984 |
| 30-007-90027 | 36.832 | -104.548 | 2324 | 1574 | 750 |
| 30-007-20038 | 36.261 | -104.521 | 1789 | 574 | 1215 |
| MARQUEZ #1 | 37.533 | -104.460 | 1897 | 2121 | -224 |
| 30-007-20057 | 36.521 | -104.445 | 1876 | 833 | 1043 |
| PRESSEY #1 | 37.775 | -104.406 | 1855 | 390 | 1465 |
| 30-033-20030 | 36.060 | -104.402 | 1840 | 666 | 1174 |
| MOORE #002 | 36.761 | -104.385 | 1905 | 1189 | 716 |

| | | | | | |
|---|---|---|---|---|---|
| 30-007-07016 | 36.761 | -104.384 | 1905 | 1189 | 716 |
| LANDON K MOORE #001 | 36.767 | -104.383 | 1908 | 1220 | 688 |
| 30-007-90053 | 36.219 | -104.383 | 1795 | 639 | 1156 |
| 30-007-07036 | 36.767 | -104.383 | 1907 | 1236 | 671 |
| PRE-ONGARD WELL #001 | 36.521 | -104.365 | 1910 | 768 | 1142 |
| STATE #1 | 37.602 | -104.336 | 1719 | 574 | 1145 |
| U S A #1 | 37.536 | -104.333 | 1733 | 1881 | -148 |
| 30-007-05007 | 36.347 | -104.328 | 1880 | 397 | 1483 |
| 30-007-20019 | 36.402 | -104.243 | 1990 | 672 | 1318 |
| 30-007-20055 | 36.779 | -104.225 | 2032 | 1120 | 912 |
| PORTER #1-28 | 38.193 | -104.223 | 1375 | 2212 | -837 |
| PRE-ONGARD WELL #001_2 | 36.473 | -104.179 | 2028 | 633 | 1395 |
| 30-007-20018 | 36.285 | -104.096 | 1859 | 695 | 1164 |
| SALT CREEK RANCH #1 | 37.178 | -104.063 | 1697 | 746 | 951 |
| TRUE STATE #23-16 | 38.046 | -104.016 | 1344 | 2002 | -658 |
| CHAMPLIN ET AL GOV #1 | 37.883 | -103.979 | 1436 | 2072 | -636 |
| JORDAN GOV #1-X | 37.908 | -103.860 | 1354 | 2056 | -702 |
| WALDROUP #1 | 37.185 | -103.849 | 1749 | 880 | 869 |
| 30-059-20045 | 36.722 | -103.744 | 1907 | 1155 | 752 |
| 30-021-20540 | 35.764 | -103.744 | 1319 | 671 | 648 |
| GOVT. CYNTHIA TRUE #1 | 37.582 | -103.730 | 1630 | 523 | 1107 |
| 30-059-20431 | 36.310 | -103.711 | 1772 | 789 | 983 |
| J W MCNALLY #1 | 37.776 | -103.673 | 1403 | 1909 | -506 |
| CRAIGHEAD #1 | 37.861 | -103.636 | 1340 | 2089 | -749 |
| DENTON B #1 | 37.465 | -103.532 | 1691 | 514 | 1177 |
| 30-059-20433 | 36.462 | -103.508 | 1677 | 1186 | 491 |
| 30-059-20005 | 36.924 | -103.447 | 1620 | 840 | 780 |
| COLORADO #B-1 | 37.481 | -103.432 | 1605 | 632 | 973 |
| USA #3253-14-12 | 37.255 | -103.335 | 1719 | 595 | 1124 |
| GOVERNMENT #1 | 37.789 | -103.325 | 1325 | 1959 | -634 |
| 30-059-20445 | 36.827 | -103.308 | 1619 | 1267 | 352 |
| STATE 3353 #36-2 | 37.132 | -103.307 | 1619 | 494 | 1125 |
| STATE #3252-16-7 | 37.259 | -103.254 | 1642 | 532 | 1110 |
| G C CAMILLI #1-9 | 37.972 | -103.248 | 1218 | 1870 | -652 |
| ETCHART #1 | 37.780 | -103.230 | 1276 | 1351 | -75 |
| M E JONES #1 | 37.657 | -103.220 | 1346 | 1335 | 11 |
| (GOV) DAVIS NCT-1 #1 | 37.624 | -103.192 | 1401 | 791 | 610 |
| BARCLAY #A-1 | 37.532 | -103.178 | 1492 | 516 | 976 |
| Dillon-1 | 37.700 | -103.151 | 1314 | 1366 | -52 |
| 30-059-20446 | 36.820 | -103.043 | 1388 | 1180 | 208 |

| | | | | | |
|---|---|---|---|---|---|
| SINGER 1 #1 | 37.031 | -103.029 | 1373 | 1391 | -18 |
| CRAMER #1 | 37.183 | -102.984 | 1513 | 987 | 526 |
| MARCI #1 | 37.245 | -102.975 | 1527 | 634 | 893 |
| CIMARRON #1 | 37.071 | -102.812 | 1375 | 1850 | -475 |

## A.3 Fault Architecture

A commonly used model for fault architecture is one where the fault is anisotropic with a low permeability core that is surrounded by a damage zone of enhanced permeability (Cain et al., 1996). A sensitivity study was conducted to evaluate the feasibility of modeling anisotropic faults, but it was found the limitation in spatial discretization and the numerical method used to solve the diffusion equation with a structured grid produced unrealistic pore pressure diffusion patterns. Instead, the faults were modeled as isotropic with bulk diffusivities to prevent erroneous numerical artifacts.

Pore pressure diffusion it not sensitive to fault orientation like poroelasticity; so the geometries used in this study are approximation based on the available data. The geometric characteristics of the three fault zones were determined based on a combination of seismicity data, moment tensors and knowledge of the regional stress regime. The geometry of the northern Trinidad fault zone was based on the combination of relocated earthquakes from the 2001 sequence (Meremonte et al., 2002; Rubinstein et al., 2014) and moment tensors (Herrmann, 2020). The fault zone was assigned a length of 10 km and a strike and dip of 33/64E. The geometry of the southern portion of the Trinidad fault zone was based on a seismological analysis of the 2011 earthquake sequence conducted by Barnhart et al. (2014). The fault zone was assigned a length of 8 km and strike and dip of 22/64E. The northern and southern portions of the Trinidad fault zone are assumed to intersect (Rubinstein et al., 2014). The Vermejo Park fault zone and Tercio fault zone geometries were based on a combination of earthquake locations from the Nakai et al. (2017) catalog and moment tensors (Herrmann, 2020).

The Vermejo Park fault zone was assigned a length of 20 km and a strike and dip of 0/60E. The Tercio fault zone was assigned a length of 9 km and a strike and dip of 355/55E.

## A.4 Fluid Properties

It has been found that fluid composition can produce a density-driven pressure transient that locally enhance vertical pressure perturbation into the basement if the injection fluid has a sufficiently higher total dissolved solids (TDS) concentration than the in-situ basement fluids (Pollyea et al., 2019, 2020). According to the U.S. Geological Survey National Produced Waters Geochemical Database (Blondes et al., 2018) the water produced from formations associated with coal-bed methane extraction has an average TDS of 2600 ppm, based on 2100 fluid samples taken within the Raton Basin. The TDS concentration of basement fluids in the Raton Basin is unknown but the National Produced Waters Geochemical Database reported basement samples from Kansas that have an average TDS around 107,000 ppm, this TDS concentration has also been utilized in other modeling studies to represent the in-situ basement fluids (Pollyea et al., 2019, 2020). Additionally, Bucher and Stober (2010) reported that most basement fluid around 5 km deep have TDS concentrations around $10^5$ ppm. Given the injection fluids likely have a lower TDS concentration than the in-situ basement fluids, it is probable that density-driven pressure transients that enhance vertical pore pressure propagation into the basement do not occur within the Raton basin, thus fluid TDS does not need to be modeled.

In terms of pressure, the Basin has been shown to be underpressured but the degree of underpressure varies from being over 1000 m underpressure in the center of

the Basin to slightly overpressured near the southeastern part of the Basin (Nelson et al., 2013). Given the large pressure ranges and lack of data in the southern and eastern portion of the model domain, a hydrostatic pressure gradient was used to calculate fluid properties. This simplification should not substantially affect calculated hydraulic diffusivities.

From a temperature point of view, the Raton Basin has been reported to have an elevated geothermal gradient (Morgan, 2009; Kelley, 2015). The geothermal gradient varies substantially from less than 20° C/km to over 100° C/km within the Basin (Morgan, 2009). Given the large range of recorded geothermal gradients, combined with lack of data for the northern and eastern portion of the model domain, a more conservative gradient of 25° C/km was used to calculate fluid properties. A sensitivity analysis was conducted to evaluate the effects of using a lower geothermal gradient when calculating the hydraulic diffusivity. It was found that when using a geothermal gradient of 46.1° C/km (Kelley, 2015) the resulting hydraulic diffusivity at 2, 3, and 5 km deep were 2.1 $m^2$/s, 0.13 $m^2$/s and 0.021 $m^2$/s, respectively. For comparison, calculated hydraulic diffusivities using the 25° C/km geothermal gradient at the 2, 3 and 5 km depths were 1.4 $m^2$/s, 0.07 $m^2$/s, 0.013 $m^2$/s, respectively. When considering the large uncertainly associated with determining hydrogeologic properties, the effects of decreasing the geothermal gradient when calculating the hydraulic diffusivity are minimal.
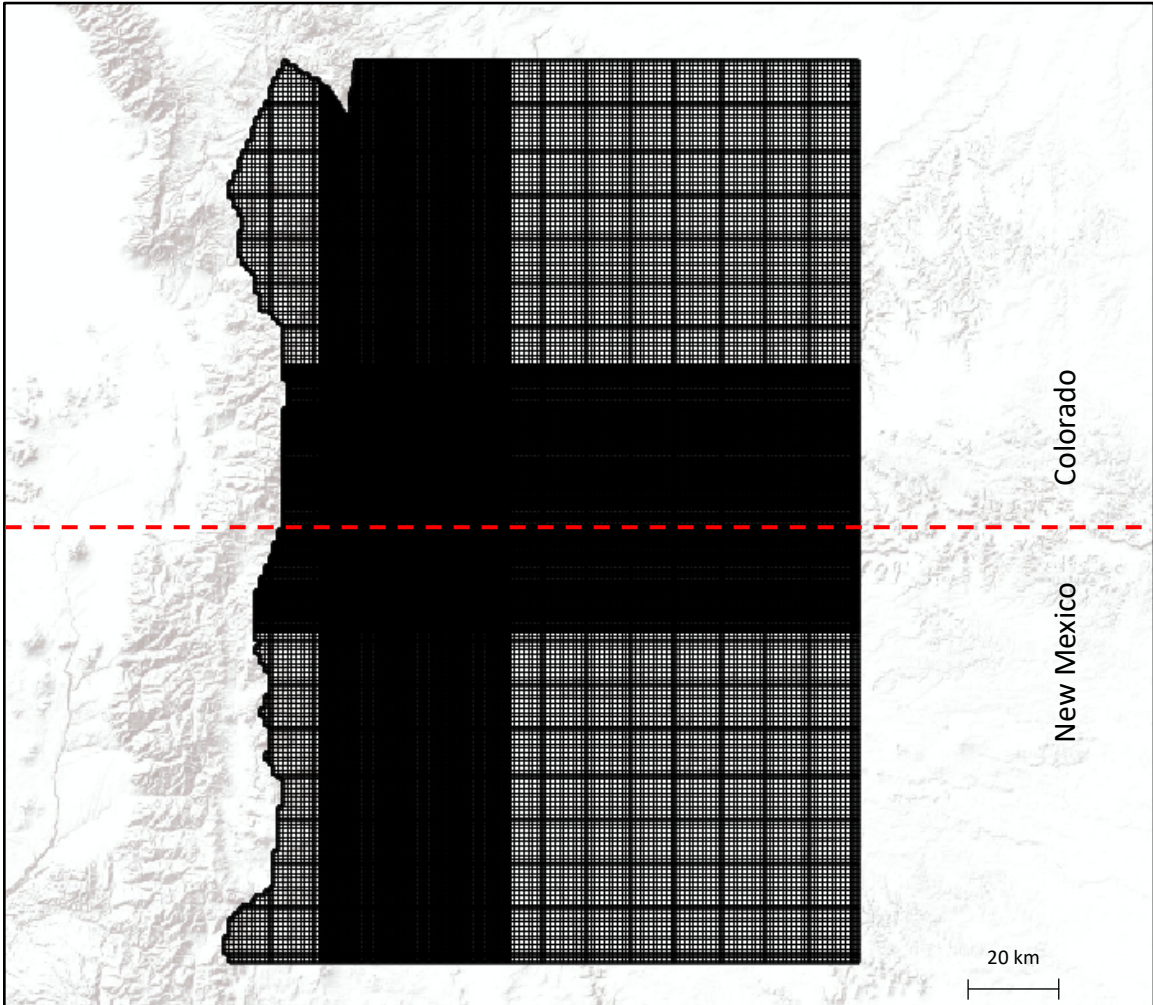
**Figure A-2.** Map view of the model domain with the finest discretization (250 m x 250 m) encompassing the injection and faulted region and coarser discretization on the outer reaches of the domain.
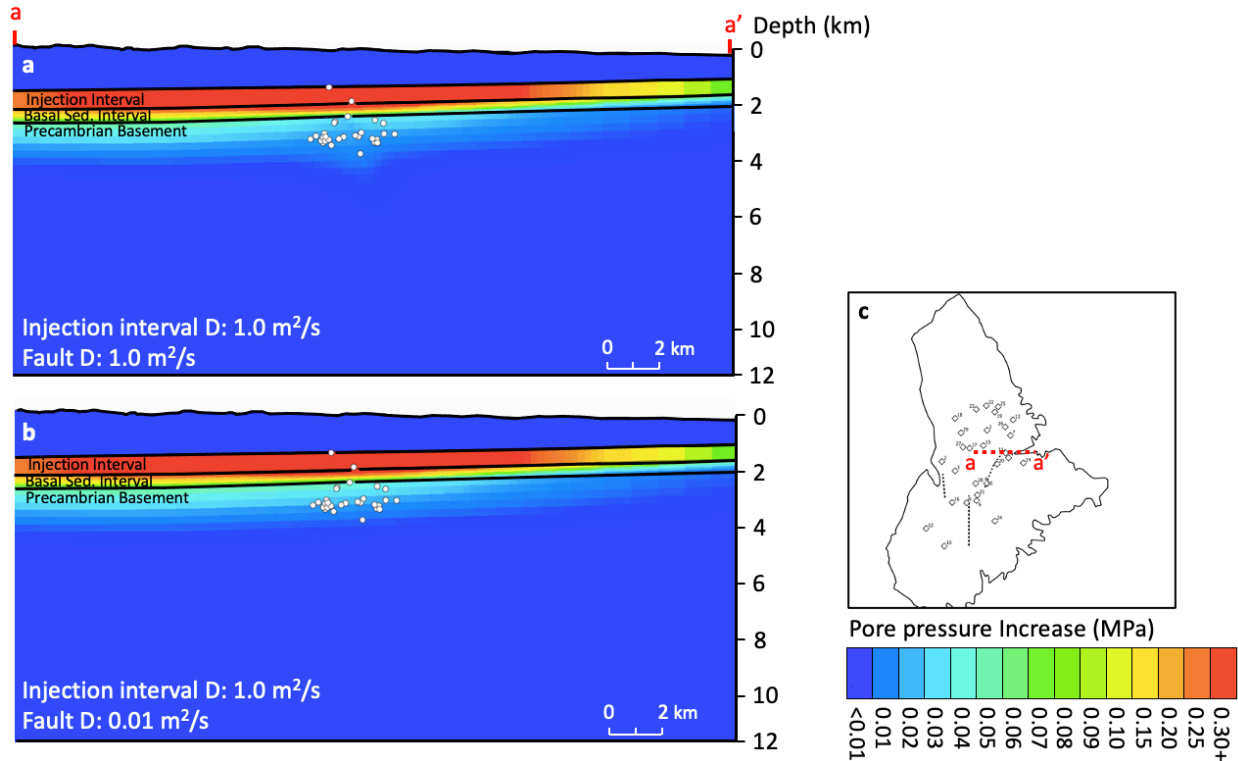
# Appendix B. Additional Model Results



**Figure B-1.** Cross sectional view of pore pressure perturbation along the N. Trinidad fault zone as of 1 September 2001. Earthquakes from September 2001 are denoted by white dots. (a) Pore pressure increase when modeling an injection interval diffusivity of 1.0 m$^2$/s and a conductive fault. (b) Pore pressure increase when modeling an injection interval diffusivity of 1.0 m$^2$/s and a sealing fault. (c) Map view showing the extent of the cross sections.
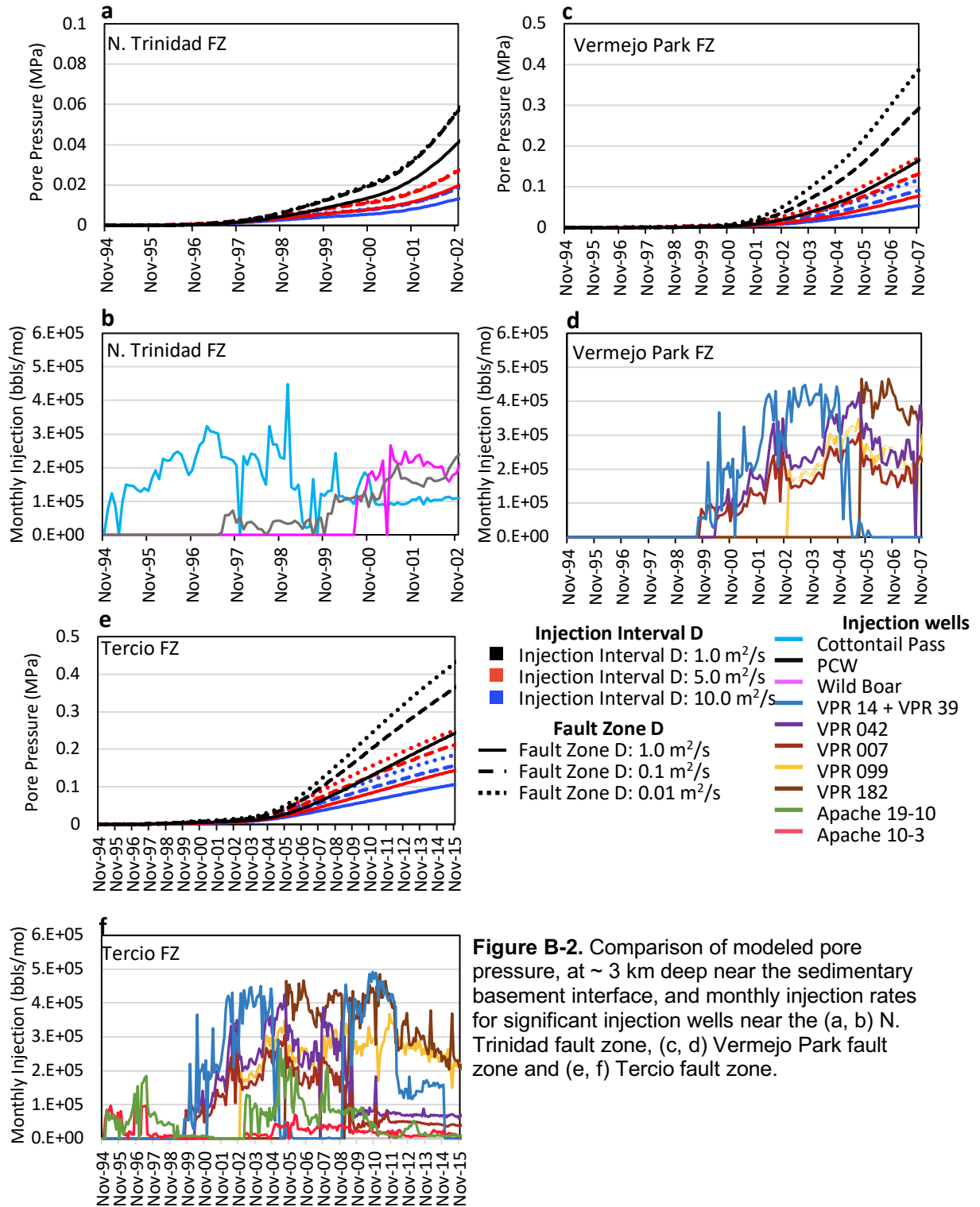
**Figure B-2.** Comparison of modeled pore pressure, at ~ 3 km deep near the sedimentary basement interface, and monthly injection rates for significant injection wells near the (a, b) N. Trinidad fault zone, (c, d) Vermejo Park fault zone and (e, f) Tercio fault zone.
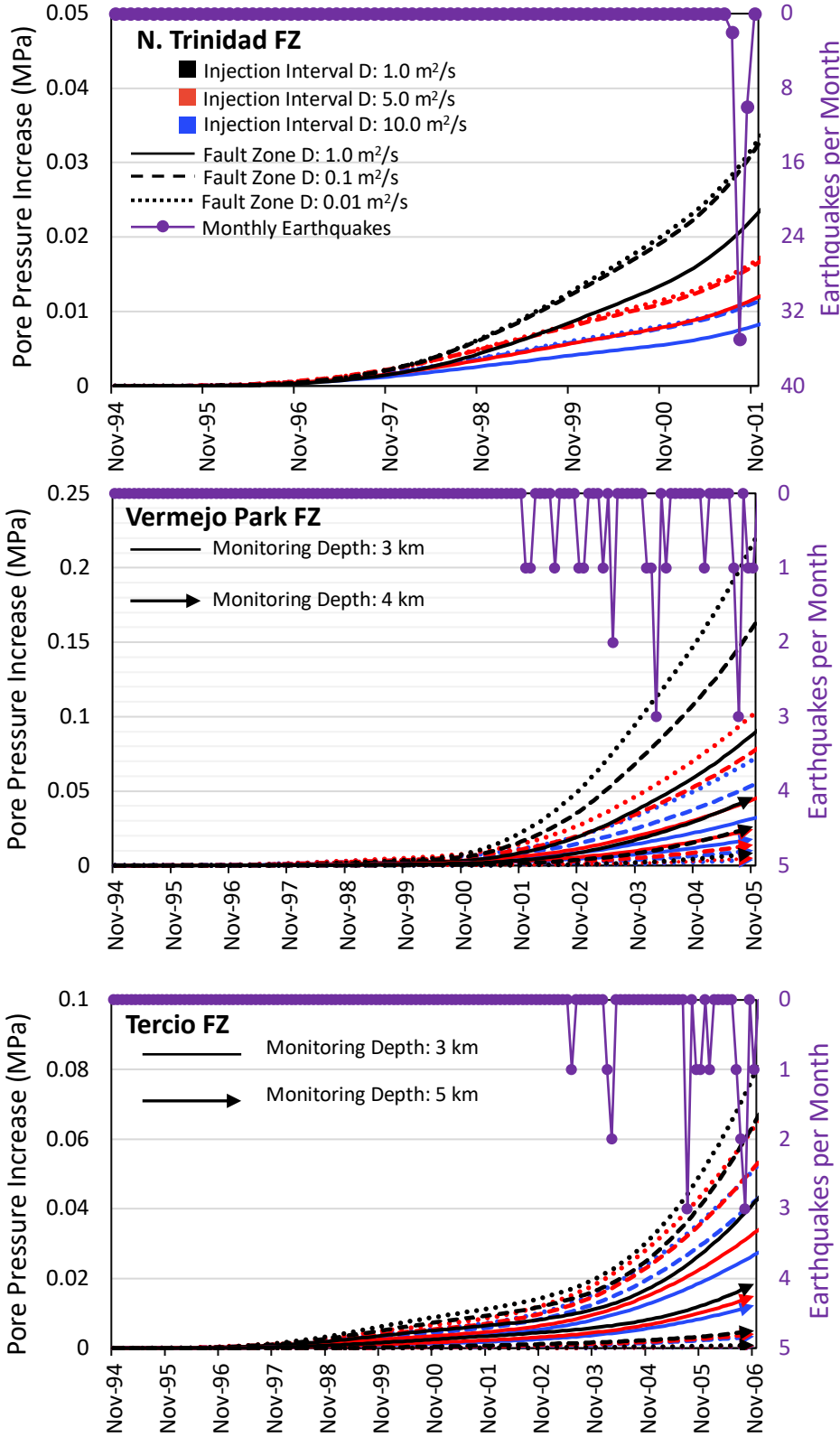
**Figure B-3.** Comparison of modeled pore pressure increase and all monthly seismicity from the Rubinstein et al. (2014) catalog within a 15 km radius of the fault zones. Pore pressure curves are colored by injection interval diffusivity and the line patterns are based on fault zone diffusivity. (a) Pore pressure increase on the northern extent of the Trinidad fault zone; monthly seismicity incorporates earthquakes located using the 2001 USGS temporary seismic array. (b) Pore pressure increase on northern extent of Vermejo Park fault zone monitored at 3 km deep (solid line) and 4 km deep (arrows). (c) Pore pressure increase at the center of Tercio fault zone monitored at 3 km deep (solid line) and 5 km deep (arrows).

61

**Table B-1. Total Injection and Average Injection Rates Through August 2001**

| Well Name | Age Number | AVG Injection (Bbls/Mo) | Total Injection (Bbls) | Injection Rate: Cumulative Injection (dimensionless) |
|---|---|---|---|---|
| COTTONTAIL PASS DISPOSAL WELL #32-33 | 1 | 165955 | 13774265 | 0.012 |
| APACHE CANYON #10-3 | 2 | 22431 | 1816919 | 0.012 |
| APACHE CANYON #19-10 | 3 | 41865 | 3391105 | 0.012 |
| PCW #12-4 WD | 4 | 72521 | 3698590 | 0.020 |
| VPR C #14 WDW | 5 | 40015 | 1000378 | 0.040 |
| VPR "A" #007 | 6 | 83065 | 1993550 | 0.042 |
| SAWTOOTH #34-4 WD | 7 | 60463 | 1088333 | 0.056 |
| VPR C #39 | 8 | 166222 | 2825770 | 0.059 |
| VPR "A" #042 | 9 | 115914 | 1970540 | 0.059 |
| VPR B #027 | 10 | 37996 | 569946 | 0.067 |
| WILD BOAR #21-32 WD | 11 | 173858 | 2434006 | 0.071 |
| VPR D #025 | 12 | 81732 | 1062521 | 0.077 |
| BEARDON #24-15 WD | 13 | 144600 | 1301401 | 0.111 |
| LONG CANYON #43-12 WD | 14 | 44495 | 266967 | 0.167 |
| LA GARITA #42-20 WD | 15 | 47202 | 94404 | 0.500 |
| VPR E #099 | 16 | 0 | 0 | 0.000 |
| WESTON #24-23 A WD | 17 | 0 | 0 | 0.000 |
| CIMARRON #32-18 WD | 18 | 0 | 0 | 0.000 |
| DEL AGUA #44-2 WD | 19 | 0 | 0 | 0.000 |
| HILL RANCH DEEP #14-12 WD | 20 | 0 | 0 | 0.000 |
| VPR "A" #182 | 21 | 0 | 0 | 0.000 |
| JAROSA #32-33 WD | 22 | 0 | 0 | 0.000 |
| FERMINIA #12-6 WD | 23 | 0 | 0 | 0.000 |
| VPR "A" #500 | 24 | 0 | 0 | 0.000 |
| SOUTHPAW #33-36 WD | 25 | 0 | 0 | 0.000 |
| POLLY #23-29 WD R | 26 | 0 | 0 | 0.000 |
| LOPEZ CANYON SWD #1 | 27 | 0 | 0 | 0.000 |
| VPR C #204 WDW | 28 | 0 | 0 | 0.000 |
| San Pablo #11-4 WD | 29 | 0 | 0 | 0.000 |

# Appendix C. Model Constraining

## C.1 Basin Underpressure and Wellhead Pressure

The Basin's injection formations are underpressured (Nelson et al., 2013), meaning the pressure in the aquifer is below hydrostatic. The wastewater disposal wells in the Raton Basin have predominantly been gravity-fed (Rubenstein et al., 2014, Nakai et al., 2017), meaning no wellhead pressure is applied. Gravity fed injection is consistent with reported underpressured injection formations (Nelson et al., 2013). However, 9 of the 29 wells have reported wellhead pressures at some point in their injection history. In theory, recording of wellhead pressure means that the formation has become overpressured and requires additional pressure beyond that produced by a hydrostatic water column to inject into the formations. When available, wellhead pressure can be used to help constrain the hydraulic diffusivity of the injection formation (e.g., Yeo et al., 2020).

The reported wellhead pressures for the Raton Basin are inconsistent. For example, the wells that reported wellhead pressure do not necessarily have the highest injection rates, nor are they located in areas of lesser underpressure. Additionally, several wells abruptly stopped reporting wellhead pressure without a significant drop of injection rate. The variability in the data is potentially a result of reporting error or neglecting to report wellhead pressure entirely.

The inconsistency of the wellhead pressure data makes it unclear if the data accurately represents the subsurface pressure conditions of the aquifer. Of the wells that reported wellhead pressures, wells VPR 39 and VPR 14 display the most realistic wellhead pressure patterns. Basin underpressure was interpolated from drill-stem data

from Nelson et al. (2013) to generate underpressure estimates at the wells (Figure C-1). The wellhead pressures were added to the underpressure estimates to estimate an upper pore pressure boundary. For eight additional moderately-high to high-rate injection wells (Cottontail Pass, Wild boar, VPR 182, VPR 042, Beardon, VPR 007, Hill Ranch and PCW; Table B-1) that did not report wellhead pressures, we used the underpressure estimate as an upper pore pressure boundary. The upper pore pressure boundaries can be compared to modeled pore pressure to help constrain the hydraulic diffusivity of the injection interval. If the modeled pore pressure was significantly higher than the upper pore pressure boundary than the hydraulic diffusivity associated with the modeled pore pressure can be ruled out.
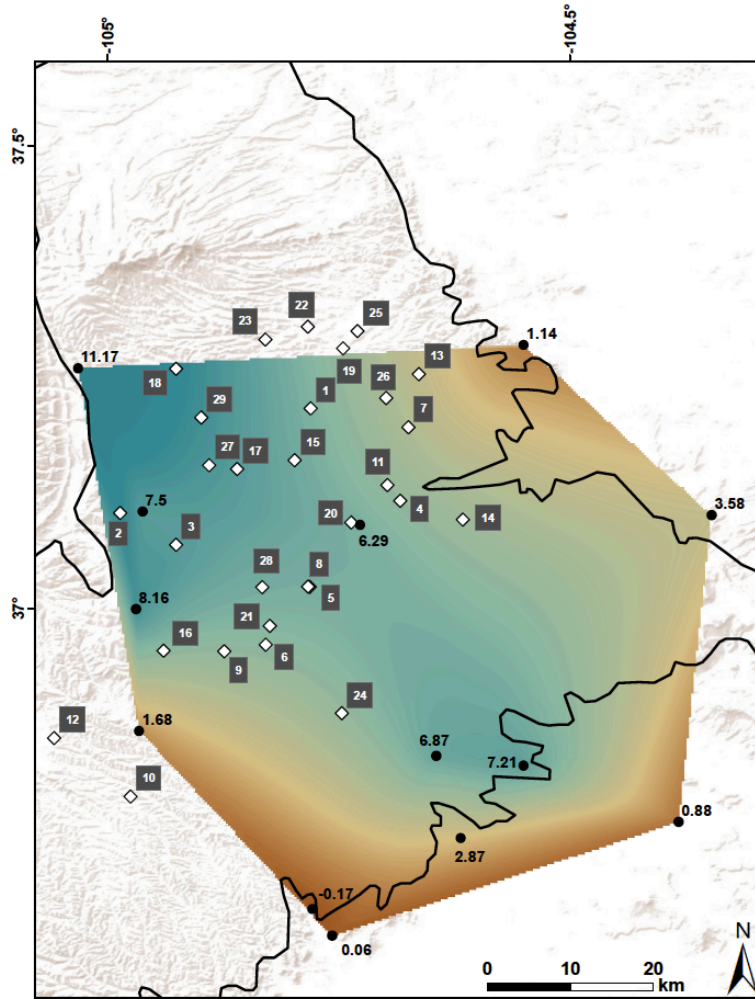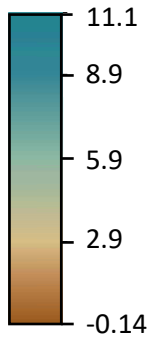
**Figure C-1.** Interpolated map of underpressure for the Dakota Formation. Black dots are drill-stem data extracted from Nelson et al. (2013) labeled with the degree of underpressure (MPa). White diamonds are injection wells labeled with the well's age number (1 = oldest well).

Underpressure (MPa)

11.1

8.9

5.9

2.9

-0.14

## C.2 Diffusivity Constraining

Pore pressure model calibration is often limited because in situ pressure measurement in the deep injection reservoirs are scarce so the pressure conditions of the reservoirs before and after injection commenced are unknown. As a proxy for in situ pressure measurements, wellhead pressure can be used to help constrain a pore pressure models (e.g., Yeo et al. 2020). As mentioned above, most injection wells in the Raton Basin are gravity feed but several wells have recorded wellhead pressures. Using the procedure outline above, we created upper pore pressure boundaries for ten injection wells within the basin. In this section we compare the modeled pore pressure increases to the estimated upper pore pressure boundaries to help constrain the diffusivity of the injection interval.
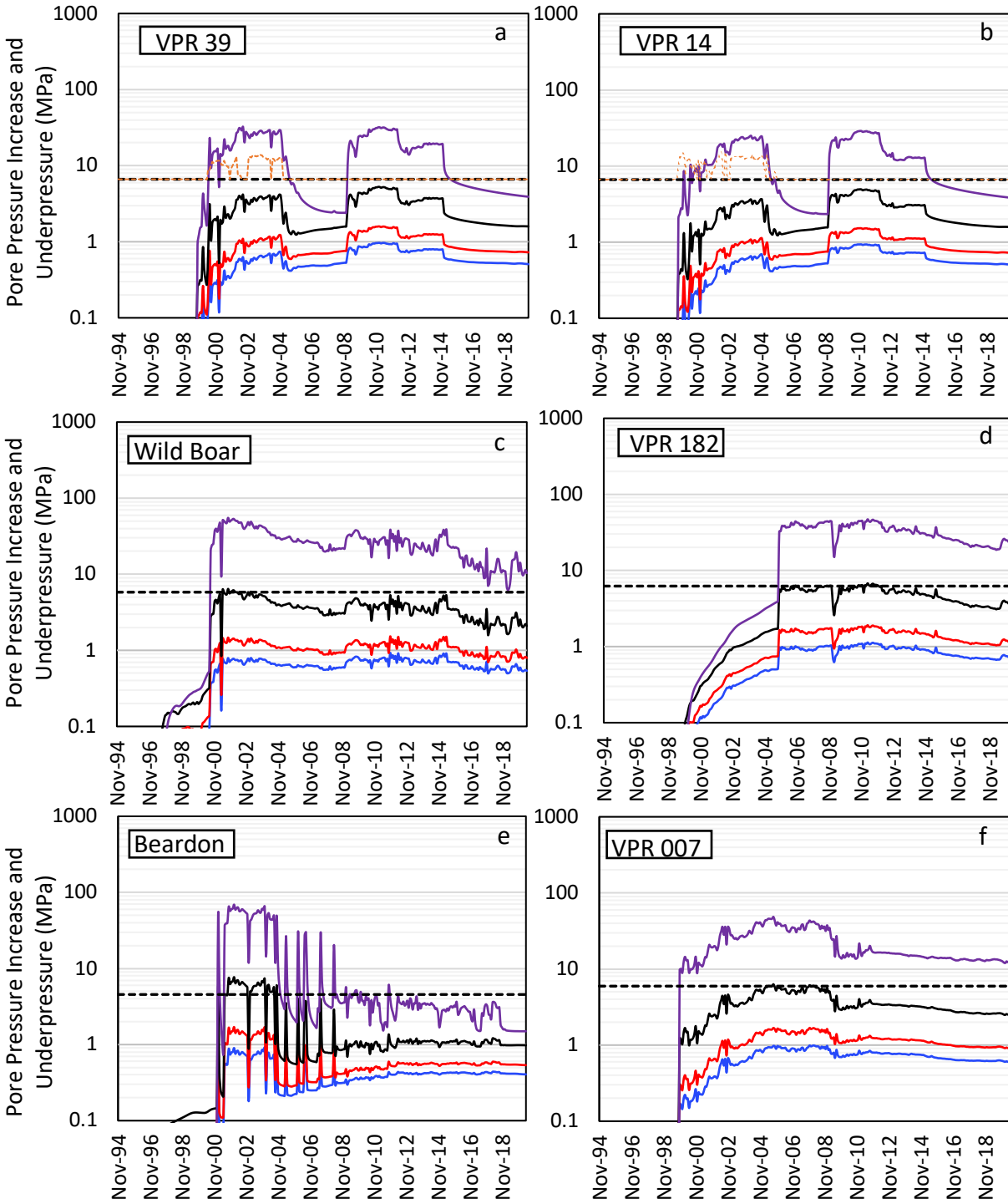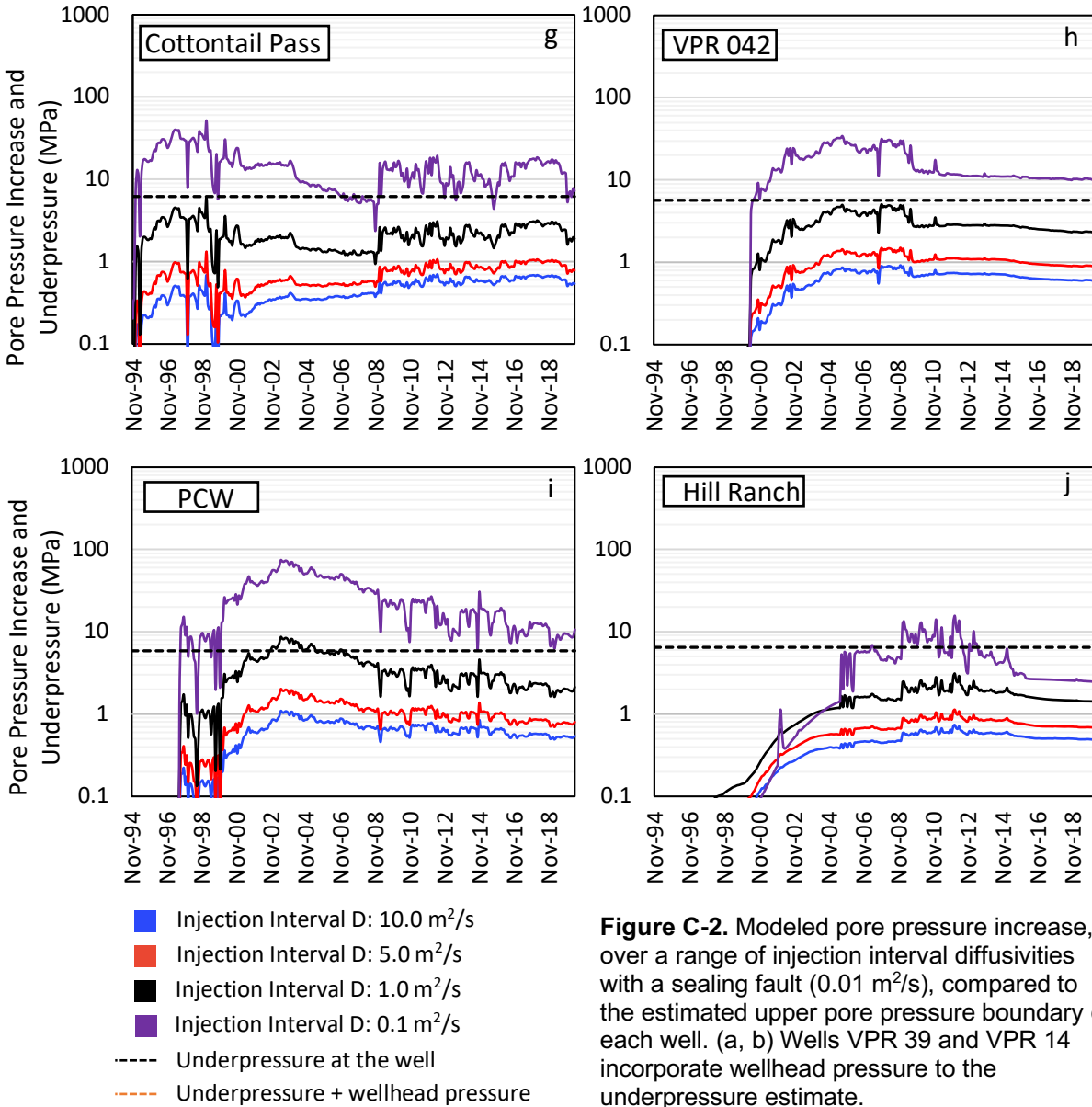
**Figure C-2.** Modeled pore pressure increase, over a range of injection interval diffusivities with a sealing fault (0.01 m²/s), compared to the estimated upper pore pressure boundary of each well. (a, b) Wells VPR 39 and VPR 14 incorporate wellhead pressure to the underpressure estimate.

# Appendix D. Sensitivity Analysis

## D.1 Injection Interval Diffusivity vs Fault Zone Diffusivity

The coefficient of variation (CV; Brown, 1998) defined by CV = $\sigma$ / $\mu$, where $\sigma$ is standard deviation and $\mu$ is mean, was used to evaluate how sensitive our pore pressure model was to varying diffusivity. The CV was calculated for two situations, (1) varying the diffusivity of the injection interval and (2) varying the diffusivity of the fault zones. The situations were divided into scenarios that had different combinations of injection interval and fault zone diffusivity (Table D-1). For each scenario three monthly CV time series were calculated, one for each depth, using modeled pore pressure from the parameter combinations in Table D-1. For the variable injection interval diffusivity situation, we have three scenarios that have three CV time series each (Table D-1), one for each depth, for a total of nine CV time series (Figure D-1a). Each times series was calculated using modeled pore pressure from four model simulations each with a different injection interval diffusivity (0.1 $m^2$/s, 1.0 $m^2$/s, 5.0 $m^2$/s, 10.0 $m^2$/s) but the same fault zone diffusivity. The CV time series was averaged over time so we could assign all the scenarios a single CV for each depth (Figure 8a). The average CV was calculated over a duration of 262 months, starting whenever the pore pressure front first reached the monitoring depth (Figure D-1a CV). This was done because CV decayed after the pore pressure front initially reached the monitoring location (Figure D-1) and we wanted to use a consistent amount of CV values for all scenarios. As a result, the starting and ending times used to calculate the average CV varied based on the scenario and depth. For the variable fault zone diffusivity situation, we have four scenarios that have three CV time series each (Table D-1), one for each depth, for a

total of twelve CV time series (Figure D-1b). Each time series was calculated using

modeled pore pressure from three model simulations each with a different fault zone

diffusivity (0.01 $m^2$/s, 0.1 $m^2$/s, 1.0 $m^2$/s) but the same injection interval diffusivity. The

CV time series were averaged in the same way as the variable injection interval

diffusivity situation except the time duration used was 282 months.

## Table D-1. Coefficient of Variation Scenarios

| Varying injection interval D with constant fault D (Figures 8a, D-1a) | | | |
|---|---|---|---|
| **Scenario** | **Injection interval D (m$^2$/s)** | **Fault zone diffusivity (m$^2$/s)** | **Depths** |
| Varying injection interval D with constant fault zone D: 1.0 (m$^2$/s) | 10 | 1 | 3 km, 4.5 km, 6 km |
| | 5 | | |
| | 1 | | |
| | 0.1 | | |
| Varying injection interval D with constant fault zone D: 0.1 (m$^2$/s) | 10 | 0.1 | |
| | 5 | | |
| | 1 | | |
| | 0.1 | | |
| Varying injection interval D with constant fault zone D: 0.01 (m$^2$/s) | 10 | 0.01 | |
| | 5 | | |
| | 1 | | |
| | 0.1 | | |
| **Varying fault zone D with constant injection interval D (Figures 8b, D-1b)** | | | |
| Varying fault zone D with constant injection interval D: 10.0 (m$^2$/s) | 10 | 1 | 3 km, 4.5 km, 6 km |
| | | 0.1 | |
| | | 0.01 | |
| Varying fault zone D with constant injection interval D:5.0 (m$^2$/s) | 5 | 1 | |
| | | 0.1 | |
| | | 0.01 | |
| Varying fault zone D with constant injection interval D:1.0 (m$^2$/s) | 1 | 1 | |
| | | 0.1 | |
| | | 0.01 | |
| Varying fault zone D with constant injection interval D:0.1 (m$^2$/s) | 0.1 | 1 | |
| | | 0.1 | |
| | | 0.01 | |

[a]There are a total of seven scenarios, three for the variable injection interval diffusivity situation and four for the variable fault zone diffusivity situation, each scenario is further divided into three depths. Each scenario for the variable injection interval diffusivity situation used four model simulations with the injection interval and fault zone diffusivity combinations listed in the row. Each scenario for the variable fault zone diffusivity situation used three model simulations with the injection interval and fault zone diffusivity combinations listed in the row.
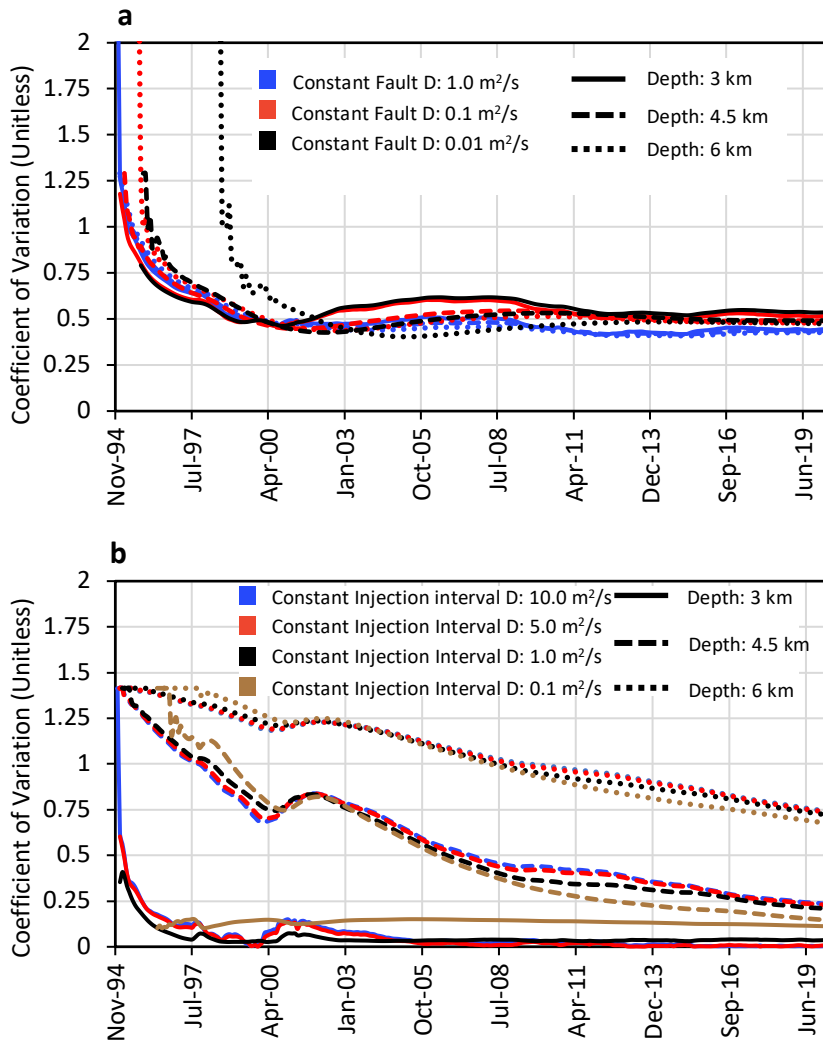
**Figure D-1.** Coefficient of variation (CV) showing the pore pressure models sensitivity to varying the diffusivity of the injection interval and fault zones. The CV was calculated at 3 km, 4.5 km, and 6 km deep on the N. Trinidad fault zone. (a) CV when varying injection interval diffusivity and keeping the fault zone diffusivity constant. (b) CV when varying the fault zone diffusivity but keeping the injection interval diffusivity constant.
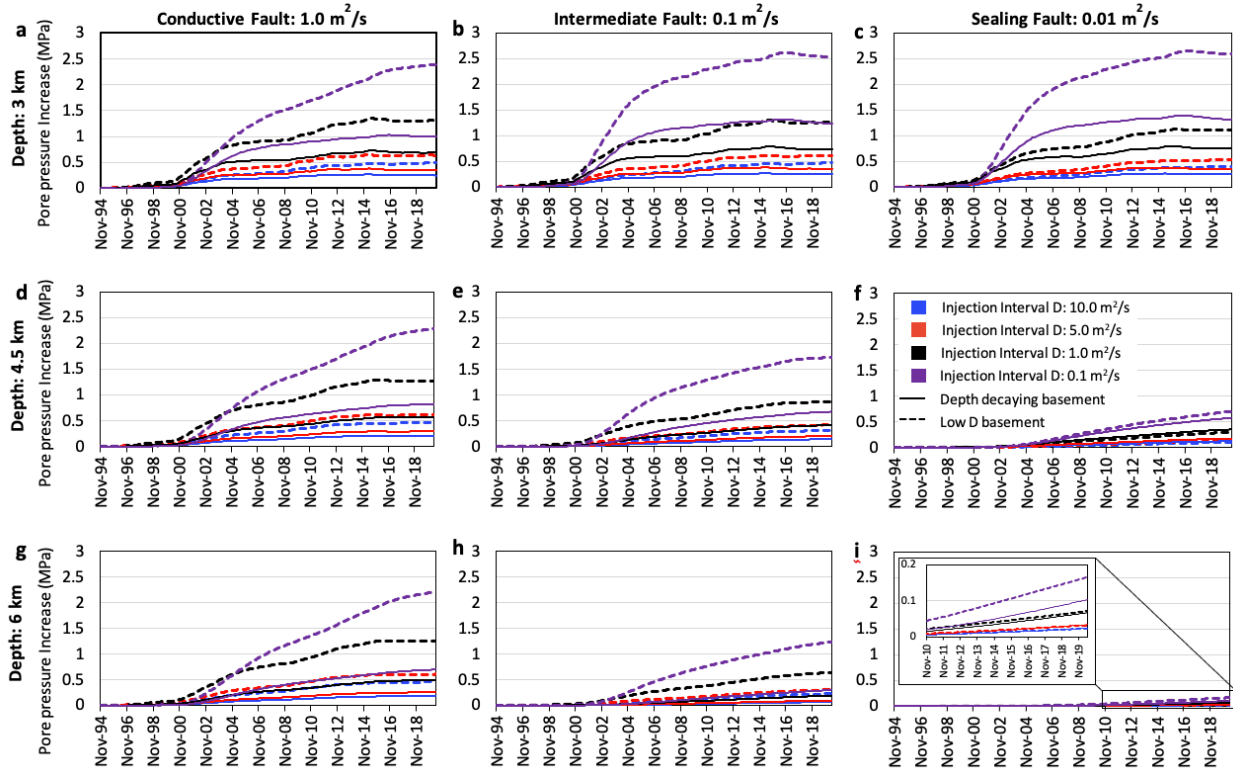
**Figure D-2.** Comparison of pore pressure increase when modeling a homogeneous low diffusivity basement (dashed lines) and a depth decaying diffusivity basement (solid lines) over a range of injection interval diffusivities (colors of lines) and fault zone diffusivities (columns). (a, b, c) Pore pressure was monitored at 3 km deep near the sedimentary-basement interface, (d, e, f) 4.5 km deep, and (g, h, i) 6 km deep.